Submitted version of paper published in Journal of Sound and Vibration 488 (2020) 115632
DOI: https://doi.org/10.1016/j.jsv.2020.115632

Dynamic wheel-rail interaction at high speed based on time-domain moving Green's functions

S. Zhang [1], G. Cheng [1], X. Sheng [2]*, D. J. Thompson [3]

[1] *State Key Laboratory of Traction Power, Southwest Jiaotong University, Chengdu, 610031, China*

[2] *School of Urban Railway Transportation, Shanghai University of Engineering Science, Shanghai, 201620, China*

[3] *Institute of Sound and Vibration Research, University of Southampton, Southampton, SO17 1BJ, UK*

**Correspondence author. Email: shengxiaozhen@hotmail.com*

Abstract

Many issues of concern in the railway industry are fundamentally caused by dynamic wheel-rail interaction. To deal with these issues, the characteristics of the interaction must be accurately predicted and fully understood; this becomes even more challenging when the train speed is high. Although much research has dealt with wheel-rail interaction, some aspects related to high speed trains still need to be further addressed. In this paper, an approach based on time-domain moving Green's functions developed previously is extended and employed to calculate wheel-rail forces. The extension includes consideration of the flexibility and rotation of the wheelset by incorporating the associated time-domain moving Green's functions in the method. These are derived from the corresponding receptances by applying an experimental modal analysis technique to the calculated frequency response functions. Cases are considered for a single, or multiple, wheelsets rolling over a track represented as an infinitely long periodic structure. Wheel-rail forces are calculated for a set of parameters typical of the Chinese high-speed railway and for a number of typical excitation cases, including purely parametric excitation on a smooth rail, an indentation on the rail, wheel polygonisation and rail corrugation, for the purpose of revealing the frequency content of high-speed wheel-rail interaction. Effects of the wheel rotation on the wheel-rail forces are studied and comparisons are made between a single wheelset and multiple wheelsets.

Keywords: wheel rotation; periodic structure; moving Green's function; wheel-rail interaction.

1. Introduction

In the past decade or so, China has constructed more than 35,000 km of high-speed railways and increased the maximum operating speed up to 350 km/h. Such a rapid development greatly benefits the country and its people, but at the same time also significantly impacts the environment by generating noise and vibration. The issues of the initiation and growth of rail corrugation and wheel out-of-roundness further worsen the situation by generating larger dynamic wheel-rail forces. The increased dynamic forces not only give rise to higher noise and vibration, but also cause damage or failure to the track structure and/or the vehicle, threatening the safety of railway operation. These issues are fundamentally caused by dynamic interaction between the wheel and the rail. Therefore, in the past, numerous wheel-rail interaction models have been established, either in the time domain or in the frequency domain, for the purpose of addressing these and other issues.

There are two basic types of wheel-rail interaction models which have been developed and applied. The first one may be termed the 'moving irregularity' model in which an irregularity strip is assumed to move between a stationary wheel and rail. Models in this category are established either in the frequency domain or in the time domain [1]. In the frequency domain the track may be truncated to a finite length but is usually considered to be an infinitely long structure [2, 3]. Beam theory [4, 5] can be used to model the track; more advanced models based on a finite element approach have also been developed [6]. The 'moving irregularity' model normally has a relatively high computational efficiency, but excludes effects related to the moving axle load and moving mass of the wheel.

The second type of model is the 'moving wheel' model in which, as in reality, the wheel is allowed to move along the track. Models in this category are usually established in the time domain. In this case, the track is normally truncated to a finite length [7-10]. However, this can cause difficulty in dealing with high speeds as the required length can become large. Thus, several 'moving wheel' models have been developed in the frequency domain [11-14] in which the track is regarded as an infinitely long periodic structure. Of the various approaches, there are two which are particularly suitable for dealing with high speeds.

In Refs. [12-14], the so-called Fourier-series approach was developed to study steady-state wheel-rail interactions generated by a single, or multiple, wheels moving along a railway track represented as an infinitely long periodic structure in the frequency domain. Wheel-rail forces are determined by solving a set of linear algebraic equations, and therefore this approach is quite computationally efficient.

However, this method requires the wheel-rail roughness also to be periodic with the period being a multiple of the track period. Moreover, it also requires the contact spring to be linearized and cannot allow for loss of contact between the wheels and the rail. For discrete wheel and rail irregularities, such as a wheel flat or a rail indentation, wheel-rail impact and loss of contact may occur and this approach is inapplicable.

The other approach that can be considered for high speeds operates in the time domain. It is based on the so-called time-domain Green's functions of the track [15-20], in which integral equations, in addition to differential equations, are solved for the wheel-rail forces. According to these references, the time-domain Green's function of the track is first calculated. Then the classic Duhamel integral equation is applied to express the response of the rail at the wheel-rail contact points due to these forces, and at the same time differential equations are established for the wheels which are modelled as rigid bodies. These equations are then coupled using wheel-rail contact conditions (normally the Hertz contact theory). The difference between Ref. [16] and Ref. [20] lies in the Green's functions used for the track. In Ref. [16] a 'stationary' Green's function is used, which is the response of the rail at a position due to an impulsive force applied at the same or another position. The motion of the wheel along the rail is accounted for by appropriately changing the response and loading positions that are sampled in the Green's functions. To do so, Green's functions have to be calculated for a sufficient number of loading and response positions within a sleeper bay. In Ref. [20], however, a moving Green's function is used and the integral equation takes into account the motion of the wheel directly.

It is noted here that in all the aforementioned models the wheel is treated either as a rigid body or an elastic body not in rotation. In the case of high speeds, wheel-rail interactions not only are of high frequency, but also complicated by the moving load effect. As a wheelset rolls at high speed over the track, it is subject to wheel-rail forces moving at the same speed along the rolling surfaces, bringing moving load effects to the dynamics of the wheelset. The rotation of the wheelset also introduces centrifugal and gyroscopic effects. It can be expected that these effects introduce additional complication and differences into the wheel-rail interactions compared with the case in which the wheelset rotation is ignored.

Some researchers have previously taken account of the rotation of the wheel or wheelset to some extent. To predict rolling noise, Thompson [21, 22] replaced the rotation of the wheel with a rotating load. He showed that the classic concept of driving point receptance can still apply for the moving load,

and therefore, a receptance-based method can be employed to determine the wheel-rail force. Due to the rotation the resonance peaks of the wheel split into two, one higher and one lower than the resonance of the non-rotating wheel. However, the structural effects of rotation, such as centrifugal stiffening or softening and Coriolis forces, were excluded.

Fayos et al. [23] presented a method for analysing the structural vibration of a solid of revolution rotating about its main axis. The method is based on two stages: 1) the displacement of the solid is split into two parts, one associated with the rotation about the main axis, and the other associated with the deformation and other small rigid motions of the solid; 2) the second part of the displacement is calculated as a linear combination of the non-rotating modes of the solid, including both deformed and rigid body modes. These non-rotating modes are computed from a 3D FE model. This method has been applied to investigate the effect of wheel rotation on high frequency vehicle-track interaction and wheel-rail forces [24, 25] in the time domain with the track being truncated to a finite length. The importance of the inclusion of wheel rotation in wheel-rail interaction is demonstrated in these works.

Since the approach in Ref. [23] relies on the non-rotating modes calculated from a 3D mesh, it is not convenient for dealing with rotating loads such as a wheel-rail force. To overcome this shortcoming, in Ref. [26], an approach based on a 2D FE mesh is presented for modelling the dynamics of a train wheel in rotation. In this approach, the displacement of the wheel is also decomposed into two parts, a rigid body motion part (including the vertical vibration of the wheel axis and the rotation about its axis) and an elastic deformation part. Partial differential equations of motion are established by applying a finite element scheme, which only requires a 2D mesh over the cross-section containing the wheel axis, and the momentum law. The elastic displacement is described in terms of cylindrical coordinates, and is a 2π-periodic function of the circumferential angle about the wheelset axis. By decomposing the elastic displacement, using Fourier series, into components at particular circumferential orders, the partial differential equations become ordinary differential equations. For a harmonic load rotating (seen from the wheelset) about the wheelset axis, these ordinary differential equations can be solved algebraically for steady-state solutions. However, only a single wheel is considered in Ref. [26], and the axis of the wheel is assumed to vibrate only vertically. In the current paper, an extension to Ref. [26] is included to cover a rotating wheelset. This extension allows the wheelset to have rigid body motion in five degrees of freedom. Similar work is presented in [27, 28]. Compared with the approach based on a 3D mesh, the one presented in Refs. [26, 28] has advantages not only in computational efficiency, but also in dealing

with rotating loads generated from wheelset-track interactions, which are stationary in space but rotate about the wheelset axis if observed from the wheelset.

From the literature review above, there are no models which take into account the flexibility, rotation and motion of the wheelset and the infinite length of the track simultaneously. Therefore, existing models may fail to reveal some of the important characteristics of wheel-rail interaction at high speeds. Correct prediction of the characteristics of wheel-rail interaction is essential, since they are often used to explain many phenomena observed in railway operations, such as wheel polygonisation and vibration amplitude modulation.

Wheel polygonisation is often observed on China's high-speed railways and various theories have been proposed to explain the generation mechanisms. Most of the theories [29-33] assume that wheel polygonisation is related to some resonances of the vehicle-track system. For example, Ref. [30] proposes that a natural mode of the bogie frame may be responsible for high-order wheel polygonisation while in Refs. [31-33] the authors point to the third mode of the track section between two wheelsets of a bogie. It is evident that, whatever the phenomenon, the correct prediction of resonance frequencies of the wheel-track system is fundamental.

Amplitude modulation is often observed in measured axle box vibration (and even interior noise) frequency spectra in which there are many distinct and equally separated peaks around a major frequency. The separation of two neighbouring peaks is equal to the sleeper passing frequency. An example will be given in Section 4.2.1. This phenomenon was also noted in Ref. [16] in which the authors pointed out that the character of modulated vibration is due to the steady-state response to parametric excitation overlapped by the wheel-rail system's vibrations induced by the roughness. These distinct and equally separated frequencies may be wrongly used as an evidence of existence of wheel polygonisation or rail corrugation frequencies.

The aim of this paper is to investigate the interaction between fast moving and rotating wheelsets and an infinitely long periodic railway track. The investigation is performed based on the time-domain moving Green's functions of the wheel and the rail, simultaneously taking into account the flexibility, rotation and motion of the wheelset and the infinite length and periodicity of the track. In Section 2, the time-domain moving Green's functions of the wheel and rail are introduced, together with the wheel-rail force calculation method developed in Ref. [20]. In Section 3, characteristics of the receptances and Green's functions for a typical Chinese wheelset and track are analysed. Wheel-rail forces are presented

in Section 4 for a set of parameters typical of the Chinese high-speed railway and for a number of typical excitation cases. These include purely parametric excitation on a smooth rail, an indentation of the rail head, wheel polygonisation and rail corrugation. Comparisons are made between results for a single wheelset and multiple wheelsets. Conclusions are summarised in Section 5.

2. The wheel-rail interaction model based on the time-domain moving Green's functions of the wheel and rail

This section introduces the wheel-rail interaction model which is based on the time-domain moving Green's functions of the wheel and the rail. This model was developed in Ref. [20] in which the wheelset was treated as a rigid body and its motion is described by Newton's second law. Here it is extended to include a flexible rotating wheelset. The wheelset and track are regarded as being symmetric about the vertical central plane of the track and for simplicity only symmetric excitation is considered. Lateral forces are neglected so that the rails are assumed to vibrate in the vertical direction. The method used for calculating the Green's function of the track is briefly introduced in Section 2.1, and that for obtaining the Green's functions of the wheelset in Section 2.2. Application of these Green's functions to determine the wheel-rail forces is formulated in Section 2.3. The system formed by a single, or multiple, wheelsets resting on the track is a mechanical system having characteristic frequencies. These characteristic frequencies may be used to interpret the predicted wheel-rail forces. An equation is given in Section 2.4 for determining these characteristic frequencies.

In what follows, a positive vertical wheel-rail force is a compressional force. A vertical force applied at the axle is directed downwards. Positive displacements of the wheelset and rail at the wheel-rail contact point are also directed downwards.

2.1 Time-domain moving Green's function of the rail

The track considered in this paper is a typical Chinese slab track, consisting of two rails, connected by fastener systems to finite length pre-stressed concrete slabs with cast-in sleepers, in turn supported on a layer of concrete-asphalt (CA) mortar, and a concrete base. Since the concrete base is very stiff, the rail pads are relatively soft and only wheel-rail interaction at high frequency is studied, the track may be simplified to be an infinitely long Timoshenko beam discretely supported at regular positions by pairs of springs representing the fastener systems, as shown in Fig. 1. The use of a spring pair can provide both translational and rotational stiffness for the rail. If the vertical stiffness of the rail pad is k_p, then the

rotational stiffness is given by $b_S^2 k_p / 12$, where b_S is the longitudinal length of the rail pad. This is achieved by implementing the two springs separated by $b_s / \sqrt{6}$. The track is periodic with the sleeper spacing *L*.

Suppose that each rail is subject to a harmonic load (vector), $\mathbf{p}_0 \mathrm{e}^{\mathrm{i}\Omega t}$, moving at speed *c* in the *x*-direction. At $t = 0$, the load is applied at the cross-section x_0 and arrives at $x_0 + ct$ at time *t*. The displacement vector of the rail at x', which is the coordinate measured from the moving load, can be written as $\mathbf{Q}(x', x_0 + ct, \Omega)\mathbf{p}_0 \mathrm{e}^{\mathrm{i}\Omega t}$ [12, 34], where the matrix $\mathbf{Q}(x', x_0 + ct, \Omega)$ is the frequency-domain moving Green's function (also termed receptance, although it is time-dependent). This matrix depends on the load frequency Ω and is a periodic function of $x_0 + ct$ with the period being *L* (the period of the track). The time-domain moving Green's function of the track can be obtained from the inverse Fourier-transform of the frequency domain Green's function matrix, i.e.

$$\mathbf{G}^{\mathrm{R}}(x', x_0 + ct, \tau) = \frac{1}{2\pi} \int_{-\infty}^{\infty} \mathbf{Q}(x', x_0 + ct, \Omega) \mathrm{e}^{\mathrm{i}\Omega\tau} \mathrm{d}\Omega . \tag{1}$$

From Eq. (1) it can be seen that the time-domain moving Green's function of the rail, $\mathbf{G}^{\mathrm{R}}(x', x_0 + ct, \tau)$, has two time arguments, *t* and τ. According to Ref. [20], $\mathbf{G}^{\mathrm{R}}(x', x_0 + ct, \tau)$ represents the response at the position $x' + x_0 + ct$ (thus the response position is moving at speed *c*) at time τ due to a unit impulse applied at position $x_0 + ct$ at $\tau = 0$. Details of the receptance matrix can be found in Refs. [12, 14, 34]. In what follows, since only the vertical vibration is considered for the rail, the time-domain moving Green's function of the rail is denoted simply by a scalar, $G^{\mathrm{R}}(x', x_0 + ct, \tau)$.

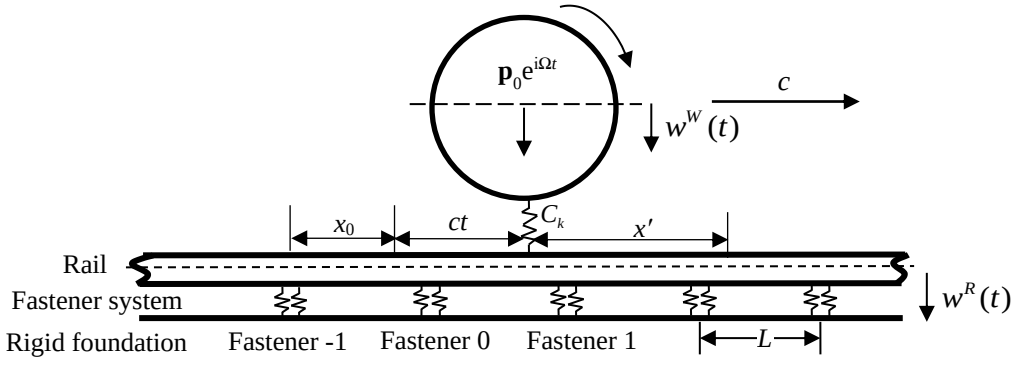

Fig. 1. A sketch of the wheel-rail interaction model.

2.2 Time-domain moving Green's function of the rotating wheelset

When a wheel rolls along the rail, the wheel is subject to a force moving around its periphery at the same speed as the train. This moving force contains not only a static component, but also dynamic components at high frequencies generated from wheel-rail interactions. The rotation of the wheelset introduces not only a moving load effect, but also centrifugal and gyroscopic effects to the wheel dynamics. However, as shown in Refs. [26, 28], for a harmonic force (e.g. a wheel-rail force), the response of the wheelset at a point fixed in a non-rotating frame (e.g. the wheel-rail contact point) is still harmonic at the same frequency as the force, even though the wheelset is rotating. This makes the concept of receptance still applicable to a rotating wheelset and the inverse Fourier transform of the receptance gives the associated time-domain Green's function, as discussed below.

Considering only vertical dynamics of the wheelset-track system and assuming symmetry at the track centreline, each wheel is subject to two forces, the vertical wheel-rail force at the wheel-rail contact point and the vertical static force acting at the axle of the wheelset. Therefore, two time-domain moving Green's functions are required for the rotating wheelset.

2.2.1 For the vertical wheel-rail forces

For a unit vertical harmonic force at the wheel-rail contact of frequency Ω, the vertical displacement of the wheelset at the wheel-rail contact point (in the same direction) can be expressed as $\tilde{Q}^{\mathrm{W}}(\Omega)\mathrm{e}^{\mathrm{i}\Omega t}$, as shown in Fig. 2(a). A special two-dimensional FE scheme is developed in Ref. [26, 28] for calculating $\tilde{Q}^{\mathrm{W}}(\Omega)$. $\tilde{Q}^{\mathrm{W}}(\Omega)$ may be split into two parts, i.e. $\tilde{Q}^{\mathrm{W}}(\Omega)=\tilde{Q}_1^{\mathrm{W}}(\Omega)+\tilde{Q}_2^{\mathrm{W}}(\Omega)$. The first part, given by $\tilde{Q}_1^{\mathrm{W}}(\Omega)=-1/(m_{\mathrm{W}}\Omega^2)$, where m_{W} is half the mass of the wheelset, represents the dynamics of the wheelset behaving like a rigid body. The second part, $\tilde{Q}_2^{\mathrm{W}}(\Omega)$, reflects the elastic and modal behaviour of the wheelset. The inverse Fourier transform of $\tilde{Q}^{\mathrm{W}}(\Omega)$ gives the time-domain (moving) Green's function of the wheelset in rotation, and this time-domain Green's function is denoted by $G^{\mathrm{W}}(t)$. The physical meaning of $G^{\mathrm{W}}(t)$ is the displacement of the wheelset at the wheel-rail contact point due to a unit ideal impulse (i.e. a delta function) applied at the wheel-rail contact point at t = 0.

Fig. 2. Wheelset load-response configurations. (a) Both excitation and response are at the wheel-rail contact points; (b) excitation is at the axle.

The time-domain Green's function can also be divided into two parts, the first part being the one in which the wheelset is treated as a rigid body and the second part representing the flexible response. The first part is given by $G_1^{\mathrm{W}}(t) = t / m_{\mathrm{W}}$, and the second part is given by $G_2^{\mathrm{W}}(t) = G^{\mathrm{W}}(t) - G_1^{\mathrm{W}}(t)$.

To produce the time-domain Green's function, it would be possible to apply a numerical Fourier transform (e.g. the FFT) on $\tilde{Q}_2^{\mathrm{W}}(\Omega)$, generating a set of discrete values for the time-domain Green's function. Here an alternative approach is adopted to obtain an analytical expression for the Green's function.

Since the wheelset is a bounded elastic body and the response of the wheelset at the wheel-rail contact point to a harmonic force is harmonic at the same frequency, it may be assumed that the response at the wheel-rail contact point is the sum of a set of 'modal' responses. According to the classical vibration theory, one may write [35]

$$\begin{aligned}\tilde{Q}_2^{\mathrm{W}}(\Omega) &= \sum_{s=1}^{R} \frac{A_s}{\Omega_s^2 + \mathrm{i}2\zeta_s\Omega_s\Omega - \Omega^2} \\ &= \sum_{s=1}^{R}\left[\frac{-A_s}{(\Omega - \mathrm{i}\zeta_s\Omega_s - \sqrt{1-\zeta_s^2}\Omega_s)(\Omega - \mathrm{i}\zeta_s\Omega_s + \sqrt{1-\zeta_s^2}\Omega_s)}\right] \\ &= \sum_{s=1}^{R} \frac{A_s}{2\sqrt{1-\zeta_s^2}\Omega_s}\left[\frac{1}{(\Omega - \mathrm{i}\zeta_s\Omega_s + \sqrt{1-\zeta_s^2}\Omega_s)} - \frac{1}{(\Omega - \mathrm{i}\zeta_s\Omega_s - \sqrt{1-\zeta_s^2}\Omega_s)}\right]\end{aligned} \tag{2}$$

where Ω_s is the sth resonance frequency of the wheelset in rotation, ζ_s is the corresponding damping ratio, A_s is the corresponding participation factor, and R is the number of resonances in the considered frequency band (0-4000 Hz in this paper). Here a resonance frequency means one at which the receptance has a peak. Since the force is moving relative to the wheelset, these resonance frequencies are generally different from the natural frequencies of the rotating wheelset, which, in general, are different from the

natural frequencies of the non-rotating wheelset mainly due to the gyroscopic effect. If Ω_s, ζ_s and A_s are known, then it can be shown that [35]

$$G_2^{\mathrm{W}}(t)=\frac{1}{2\pi}\int_{-\infty}^{\infty}\tilde{Q}_2^{\mathrm{W}}(\Omega)\mathrm{e}^{\mathrm{i}\Omega t}\mathrm{d}\Omega=\begin{cases}\sum_{s=1}^{R}\dfrac{A_s}{\Omega_s\sqrt{1-\zeta_s^2}}\mathrm{e}^{-\zeta_s\Omega_s t}\sin(\sqrt{1-\zeta_s^2}\Omega_s t), & t\geq 0;\\ 0, & t<0.\end{cases} \tag{3}$$

Thus, the time-domain Green's function of the rotating wheelset at the wheel-rail contact point is

$$G^{\mathrm{W}}(t)=\begin{cases}-t/m_W+\sum_{s=1}^{R}\dfrac{A_s}{\Omega_s\sqrt{1-\zeta_s^2}}\mathrm{e}^{-\zeta_s\Omega_s t}\sin(\sqrt{1-\zeta_s^2}\Omega_s t), & t\geq 0;\\ 0, & t<0.\end{cases} \tag{4}$$

Since $G^{\mathrm{W}}(t)$ is real, A_s must be real as well.

If the receptance has been calculated with a sufficiently fine frequency resolution, Ω_s, ζ_s and A_s can be determined by applying an experimental modal analysis (EMA) technique to the predicted receptance. After obtaining the resonance frequencies and damping ratios, the participation factors can be obtained with the imaginary parts of Eq. (2) evaluated at the rth resonance frequency, where $r = 1, 2, \ldots, R$:

$$\sum_{s=1}^{R}\frac{-2\zeta_s\Omega_s\Omega_r A_s}{[\Omega_s^2-\Omega_r^2]^2+(2\zeta_s\Omega_s\Omega_r)^2}=\mathrm{Im}(\tilde{Q}_2(\Omega_r)). \tag{5}$$

It can be seen that Eq. (5) is a set of linear algebraic equations.

Due to the fact that a train wheelset is normally very lightly damped and sharp peaks appear in $\tilde{Q}_2^{\mathrm{W}}(\Omega)$, the receptance must be calculated at a very fine frequency resolution. The frequency resolution may be determined based on the 'half-power bandwidth' defined by the resonance frequencies and material damping (for a resonance frequency Ω_s, the half-power bandwidth is given by $\eta_s\Omega_s$, where η_s is the loss factor of the material [35]). It may take a very long time to calculate the receptance at such a fine frequency resolution. It may be sped up in a way described as below. First of all, all the possible resonance frequencies within the pre-defined frequency range are calculated. According to Ref. [26, 28], resonance may occur when the load frequency is equal to $\omega_{nm}-m\Omega_y$, where ω_{nm} is a natural frequency of the rotating wheelset at circumferential order m and Ω_y is the rotation speed in radians per second. The natural frequencies of the rotating wheelset can be determined by solving an eigen-

value problem at a much cheaper cost. The receptance is calculated at and around each resonance frequency with a fine frequency resolution while elsewhere, it is calculated at a less fine frequency resolution.

2.2.2 For the vertical forces applied at the axle boxes

The wheelset is also subject to half the axle load at each axle box (this becomes a dynamic force if the bogie frame and primary suspension are taken into account), shown in Fig. 2(b). The vertical response of the wheelset at the wheel-rail contact point due to a unit impulse force applied at each axle box is denoted by $G^{\mathrm{O}}(t)$. Similar to Eq. (3), $G^{\mathrm{O}}(t)$ can be expressed to be

$$G^{\mathrm{O}}(t)=\begin{cases} t/m_W+\sum_{s=1}^{R_O}\dfrac{B_s}{\Omega_{so}\sqrt{1-\zeta_{so}^2}}\mathrm{e}^{-\zeta_{so}\Omega_{so}t}\sin(\sqrt{1-\zeta_{so}^2}\Omega_{so}t), & t\geq 0;\\ 0, & t<0. \end{cases} \tag{6}$$

Since a mode excited by the loads at the wheel/rail contact points is not necessarily excited when the loads are applied at the axle boxes, the *s*th resonance frequency is denoted here by Ω_{so}, and the number of modes in Eq. (6) is assumed to be R_O.

The time-domain Green's function of the wheelset is also calculated in Ref. [18]. In that reference, modal masses that are required in the calculation of the time-domain Green's function are estimated using both the resonance and anti-resonance frequencies of the wheelset. However, in Ref. [18] the two wheels are treated as rigid bodies.

2.3 The time domain wheel-rail interaction model

The time domain wheel-rail interaction model proposed in Ref. [20] is extended in this section to include the wheelset flexibility. The formulation is similar to that in Ref. [20] except that now to calculate the displacement of the wheelset at the wheel-rail contact point a convolution integral (Duhamel integral) of the Green's functions and forces applied to the wheelset is required, rather than using the Newton's second law for a rigid wheel. This is explained below.

It is assumed that there are *M* wheelsets moving along the track. The mass of the *k*th wheelset is denoted by $2m_k$, and its initial longitudinal position is defined by a_k, where $k=1,\ 2,\ \ldots, M$. The vertical wheel-rail force between the *k*th wheel and the rail is denoted by $F_k(t)$, which contains a static component, P_{k0}, that is half the axle load, and a dynamic component $f_k(t)$. The vertical displacement of the *k*th wheel

at the wheel-rail contact point is denoted by $w_k^{\mathrm{W}}(t)$, and that of the rail is denoted by $w_k^{\mathrm{R}}(t)$, both directed downwards. The wheel-rail irregularity at position *x* is denoted by $z_k(x)$. The sign of the rail irregularity is defined as positive if the rail surface is at a higher level than the nominal level. The sign of the wheel irregularity is defined as positive if the radius of the wheel is larger than its nominal one.

The rail displacement at the *k*th wheel-rail contact point can be calculated by the Duhamel integral (Eq. (9) in Ref. [20])

$$w_k^{\mathrm{R}}(t) = \sum_{j=1}^{M} \int_{-\infty}^{t} G^{\mathrm{R}}(a_k - a_j, a_j + ct, t-\tau) F_j(\tau) \mathrm{d}\tau \,. \tag{7}$$

Similarly, the displacement of the *k*th wheel at the wheel-rail contact point can be calculated as

$$w_k^{\mathrm{W}}(t) = \int_{-\infty}^{t} [G_k^{\mathrm{O}}(t-\tau) P_{k0} - G_k^{\mathrm{W}}(t-\tau) F_k(\tau)] \mathrm{d}\tau \,. \tag{8}$$

in which the Green's functions of the *k*th wheelset are denoted by $G_k^{\mathrm{O}}(\tau)$ and $G_k^{\mathrm{W}}(\tau)$. The minus sign before $G_k^{\mathrm{W}}(\tau)$ is due to the definitions of the force and displacement directions.

If the Hertzian contact theory is used to model wheel-rail contact, then a third equation can be established

$$w_k^{\mathrm{W}}(t) - w_k^{\mathrm{R}}(t) + z_k(a_k + ct) = C_k (F_k(t))^{2/3}, \quad \text{for } F_k(t) > 0 \,. \tag{9}$$

where C_k is a constant determined by the radius, R_k, of the *k*th wheel which can be given by the empirical expression [36]

$$C_k = 3.86 R_k^{-0.115} \times 10^{-8} (\mathrm{m/N}^{2/3}) \,. \tag{10}$$

Insertion of Eqs. (7) and (8) into Eq. (9) gives

$$\int_{-\infty}^{t} [G_k^{\mathrm{O}}(t-\tau) P_{k0} - G_k^{\mathrm{W}}(t-\tau) F_k(\tau)] \mathrm{d}\tau - \sum_{j=1}^{M} \int_{-\infty}^{t} G^{\mathrm{R}}(a_k - a_j, a_j + ct, t-\tau) F_j(\tau) \mathrm{d}\tau + z_k(a_k + ct) = C_k (F_k(t))^{2/3}, \tag{11}$$

where $k = 1, 2, \ldots M$.

Eq. (11) is a set of integral equations with the wheel-rail forces being unknowns. The number of unknowns is exactly the same as the number of the integral equations. This set of integral equations can be solved through a time-stepping process, as explained in the Appendix.

2.4 Characteristic frequencies of the wheelset-track system

If the displacement of the rail at the *l*th wheel-rail contact point due to a unit wheel-rail force at the *j*th wheel-rail contact point is denoted by $r_{lj}^{\mathrm{R}}(\omega)$, the receptance of the *l*th wheelset at the wheel-rail contact point is denoted by $r_l^{\mathrm{W}}(\omega)$, and the *l*th wheel-rail force is denoted by $\tilde{f}_l(\omega)$, then the condition that the wheel and rail are always in contact requires

$$-r_l^{\mathrm{W}}(\omega)\,\tilde{f}_l(\omega)-\sum_{j=1}^{M} r_{lj}^{\mathrm{R}}(\omega)\,\tilde{f}_j(\omega)-\frac{\tilde{f}_l(\omega)}{k_l^{\mathrm{H}}}=0,\ (l=1,2,\cdots,M), \tag{12}$$

where *M* is the number of wheelsets, and k_l^{H} is the stiffness of the *l*th contact spring. If the determinant of the coefficient matrix of Eq. (12) is zero at a frequency ω, there is a non-zero solution for the wheel-rail forces. This frequency is a characteristic frequency of the wheelset-track system. For a single wheelset, a zero determinant of the coefficient matrix of Eq. (12) means that the combined receptance of the wheel, the rail and the linearized contact spring vanishes. Since the track is an infinitely long periodic structure, it always dissipates power by transmitting the power outwards. In other words, the determinant of the coefficient matrix of Eq. (12) can never be exactly zero. So, the minimums of the smallest singular value of the coefficient matrix may be used to identify characteristic frequencies for the wheelset-track system. This will be demonstrated in Section 4.

3. Receptances and Green's functions of a typical wheelset and track

In this section, receptances and Green's functions are produced for a typical wheelset and track. Parameters for the track and the wheelset are given in Section 3.1. To assist in discussing the frequency content of the wheel-rail forces (see Section 4), receptances of the wheelsets and the track are first given in Section 3.2. The time-domain moving Green's functions of the wheelset and the rail are calculated based on these receptances in Section 3.3 and then analysed in Section 3.4.

3.1 Parameters for the track and wheelset

Parameters representing half the track structure are listed in Table 1. They are derived from design documents and in-situ testing. Since the rail pad is highly damped, the viscous damping model is used to avoid non-causal response [37]. The damping coefficient is c_{P} = 7535 Ns/m. Damping is introduced into the model by using complex stiffness in which the loss factor η_{P} is proportional to the equivalent

frequency, $\omega = \Omega - \beta c$, where Ω is a load frequency, β is a wavenumber and c is the load speed, i.e. $\eta_{\mathrm{p}} = \mu(\Omega - \beta c)$, where $\mu = c_{\mathrm{p}} / k_{\mathrm{p}} = 1.37 \times 10^{-4}$ s.

Calculation of the time-domain moving Green's function for the rail requires several parameters to be predefined, including the number of terms j which should be included in the series, the range of wavenumber β, the wavenumber spacing $\Delta\beta$, the range of load frequency Ω and the load frequency spacing $\Delta\Omega$. Here for the track parameters listed in Table 1, these parameters are determined as follows: $-15 \le j \le 15$, $-25.12 \le \beta \le 25.12$ rad/m, $\Delta\beta = 0.0025 \times 2\pi$ rad/m, $-4000 \le \Omega / 2\pi \le 4000$ Hz and $\Delta\Omega = 0.5 \times 2\pi$ rad/s. The load frequency resolution is taken to be 0.5 Hz.

It can be seen that there are 16000 load frequencies and 3200 wavenumbers at which responses of the rail in the frequency-wavenumber domain are produced, forming a matrix of order 16000×3200. The 2D inverse Fourier transform is performed on the matrix via the FFT technique, generating a matrix of the same order in the time-space domain. This matrix contains the time-domain moving Green's function, $G^{\mathrm{R}}(x', x_0 + ct, \tau)$, of the rail at particular spatial positions and time instants. According to the principle of the FFT, the Green's function is available between $x' = -200$ m and 200 m at a spacing $\Delta x' = 0.125$ m, and between $\tau = -1$ s and 1 s at a spacing $\Delta\tau = 1.25 \times 10^{-4}$ s. For a train running at 400 km/h, the sleeper passing time is 5.85×10^{-3} s, which is more than 46 times $\Delta\tau$, and a wheel will travel about 170 sleeper bays in 1 s. The Green's function at other positions and times is estimated via linear interpolation.

As indicated in the Appendix, to solve the integral equation (i.e. Eq. (11)) a time step Δt must be chosen. The choice of Δt should be such that it can sufficiently resolve the required time-domain moving Green's functions. In this paper, $\Delta t = 6.25 \times 10^{-5}$ s, ensuring a sampling frequency of 16000 Hz.

Table 1 Parameters for the track

Density of rail material	ρ = 7850 kg/m^3
Young's modulus of rail material	$E = 2.1 \times 10^{11}$ N/m^2
Shear modulus of rail material	$G = 0.81 \times 10^{11}$ N/m^2
Cross-sectional area of the rail	$A = 7.69 \times 10^{-3}$ m^2
Bending second moment of area of the rail	$I = 30.55 \times 10^{-6}$ m^4
Shear coefficient of the rail cross-section	κ = 0.4
Vertical stiffness of the rail pad	$k_{\mathrm{P}} = 5.5 \times 10^7$ N/m
Damping coefficient of the rail pad	c_{P} = 7535 Ns/m
Fastener spacing	L = 0.65 m
Width of the rail pad	b_{S} = 0.25 m

According to Refs. [26, 28], the receptance of the rotating wheelset can be calculated based on a 2D FE mesh which is shown in Fig. 3 with 2158 nodes. The mass of the wheelset is 1105.2 kg and its rolling

radius is 0.43 m. Its density is 7850 kg/m^3, Young's modulus is 210 GPa and Poisson's ratio is 0.3. To calculate the receptance of the wheelset, material damping should be provided. Since the wheelset is lightly damped, for simplicity a constant loss factor of 0.002 is assumed based on modal testing results; this is introduced through a complex Young's modulus. Half of the axle load is 80 kN.

As described in Section 2.2, to calculate the time-domain moving Green's function for the wheelset, the associated receptances of the rotating wheelset must be calculated first. This requires the determination of the number of circumferential orders to be included [26, 28]. It is found that for the frequency range considered in this paper, inclusion of circumferential orders between -10 to 10 is sufficient. A frequency resolution of 0.5 Hz is used between 10 Hz and 2000 Hz and 1 Hz between 2000 Hz and 4000 Hz. The finer frequency resolution used at low frequency is required to give improved estimates of the damping ratio for the wheelset in rotation.

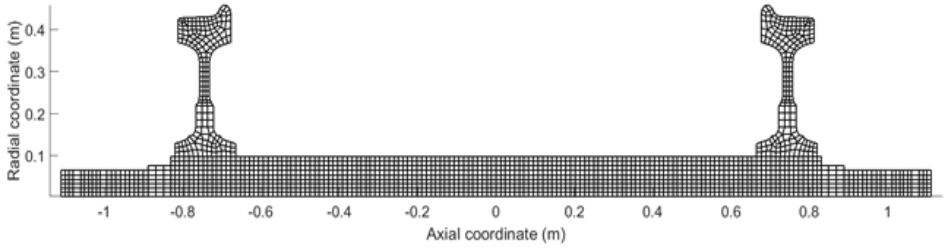

Fig. 3. The 2D finite element mesh of the wheelset.

3.2 Receptances of the wheelset and rail

Fig. 4 shows the vertical rail receptance at the loading point (at mid-span) for a stationary load and for the load moving at 400 km/h. Here for the moving load, the 'receptance' is the response of the rail at the mid-span when the load is also there. Also shown are the vertical receptance at the wheel-rail contact point of the wheelset not in rotation and that of the wheelset rotating at 400 km/h (the corresponding rotation frequency is 41 Hz).

These results indicate that the effects of wheelset rotation can be neglected when the frequency is below about 70 Hz, and the wheelset may be treated as a rigid body. Most of the peaks in the receptance of the non-rotating wheelset are split into two peaks by the rotation. The splitting is a combined effect of the moving load and wheel rotation. The amplitude of the split peaks is reduced to some extent compared with those without considering the wheel rotation.

For the track, the main effect of the moving load is to split the peak at the pinned-pinned frequency (about 940 Hz) into two. The broad peak at about 190 Hz is the rail-on-pad resonance. This peak is shifted to a lower frequency and flattened to some extent by the load speed; at this speed the sleeper-passing frequency is at around 171 Hz.

The intersection point of the wheel and rail receptances is at about 68 Hz, which is commonly known as the P2 frequency. At this frequency, the combined receptance of the wheel, the rail and the linearized contact spring (which is about 6.58×10^{-10} m/N) reaches a minimum (see Section 4.3). Below this frequency, the wheel has a greater receptance than the rail, whereas at higher frequencies up to 2000 Hz, the rail has a higher receptance than the wheel except for a few resonance frequencies of the wheelset. The receptance of the contact spring exceeds that of the rail above 1 kHz.

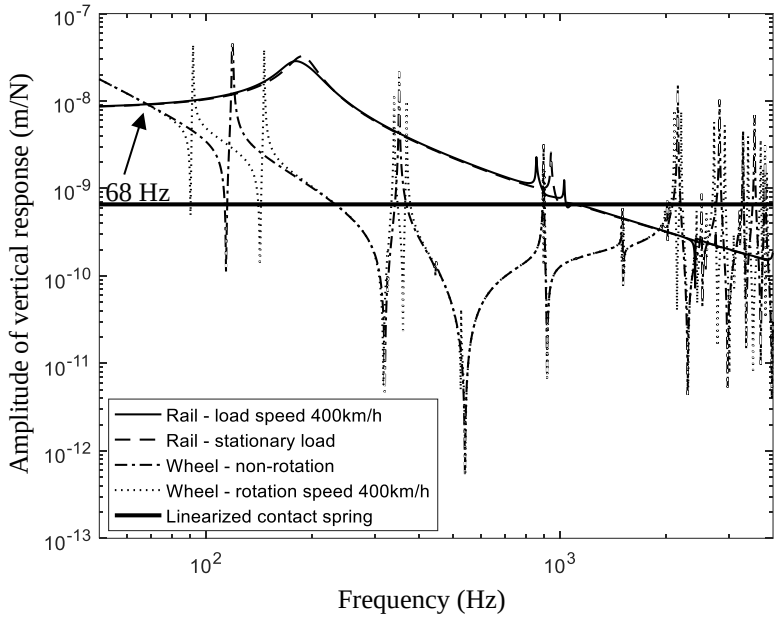

Fig. 4. Vertical receptance of the rail at the mid-span and that of the wheel at the wheel-rail contact point.

Fig. 5 shows the amplitude and phase of the vertical displacement (receptance) of the wheelset at the wheel-rail contact point due to a unit vertical force applied at each of the wheel-rail contact points (in solid line) and a unit vertical force applied on each of the axle boxes (in dashed line). The wheelset is rotating at 400 km/h. It can be seen that the two curves overlap each other below about 70 Hz, where the wheelset behaves like a rigid body. For higher frequencies, these two curves are quite different, not only in amplitude, but also in phase. It can be seen from Fig. 5(a) that, for frequencies above about 1000 Hz, the vertical displacement of the wheelset at the wheel-rail contact point due to the unit force applied

at the wheel-rail contact point is much greater than that due to the unit force applied at the axle box. The phases are quite different between these two cases. For these frequencies modes local to the wheel play a more important role, whereas for excitation at the axle box only the modes involving the bending of the axle are excited. Below 1000 Hz, the bending modes of the axle are more important than other modes. As a result, both the two curves have prominent peaks at the frequencies of modes mainly involving axle bending, but the height of the peaks on the solid curve (due to forces at wheel-rail contact points) is lower than that of the corresponding peaks on the dashed curve.

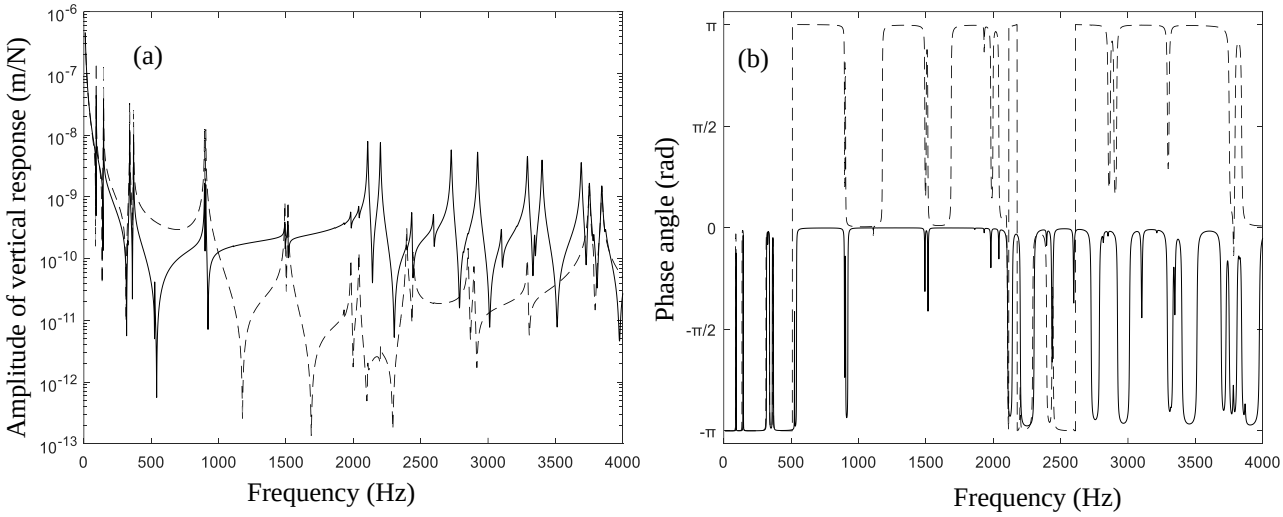

Fig. 5. Amplitude (a) and phase (b) of the vertical displacement of the wheel at the wheel-rail contact point. ——, vertical unit forces applied at the wheel-rail contact points; – – –, vertical unit forces applied on the axle boxes. The wheelset is rotating at 400 km/h.

3.3 Time-domain moving Green's function of the rail

Fig. 6(a) and Fig. 7(a) show the time-domain moving Green's function of the rail $G^{\mathrm{R}}(x', x_0 + ct, \tau)$ (as function of τ) for two response points, given by x' = 0 m and x' = 5 m, respectively, with load speed c = 400 km/h, and loading acting at $x_0 + ct$ = 0.325 m. Here, $x_0 + ct$ = 0.325 m means that at $\tau = 0$ the loading point is at mid span; x' = 0 means that at $\tau = 0$ the response position is the same as the loading position, and x' = 5 m means that at $\tau = 0$ the response position is 5 m ahead of the loading position. A time required for the disturbance to travel to the response point is clearly shown in Fig. 7(a). It is also observed that the response shown in Fig. 7(a) contains components of higher frequencies compared with that shown in Fig. 6(a).

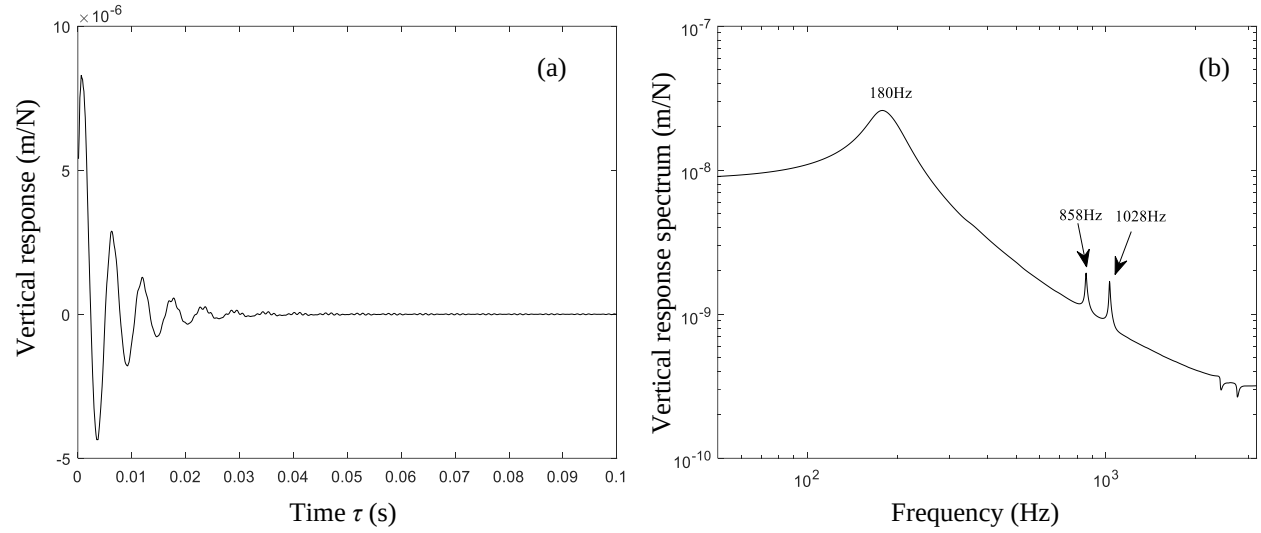

Fig. 6. Moving Green's function for rail vertical vibration with load speed 400 km/h. x_0+ct = 0.325 m and x' = 0 m. When $\tau = 0$ both the loading and response positions are at mid-span. (a) Time-history; (b) frequency spectrum.

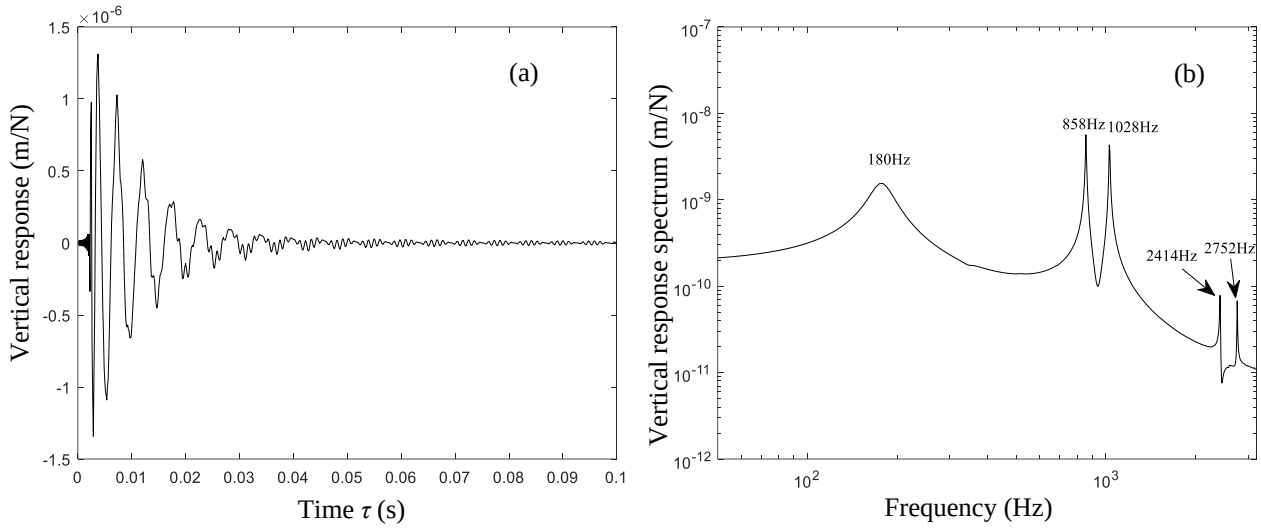

Fig. 7. Moving Green's function for rail vertical vibration with load speed 400 km/h, x_0+ct = 0.325 m and x' = 5 m. When $\tau = 0$ the loading position is at mid-span. (a) Time-history; (b) frequency spectrum.

The corresponding frequency spectra are shown in Fig. 6(b) and Fig. 7(b) at a frequency resolution of 2 Hz. The frequency spectrum in Fig. 6(b) is very similar to the instantaneous one in Fig. 4. The one in Fig. 7(b) is lower at all frequencies due to the decay of vibration along the track. The two spectra both exhibit a peak at about 180 Hz (the rail-on-pad resonance frequency modified by the load speed). Other frequency components can also be seen in these two figures, at the first and second pinned-pinned frequencies of the track split by the load speed (about 858 and 1028 Hz and about 2414 and 2752 Hz).

The peaks at 858 Hz and 1028 Hz are more pronounced in Fig. 7(b) than in Fig. 6(b) suggesting that the track decay rate at the pinned-pinned frequency is low.

3.4 Time-domain moving Green's function of the wheelset

In Fig. 4 a series of lightly damped resonances of the wheelset can be seen, which suggests that the resonance frequencies of the wheelset can be easily obtained by identifying the peaks of the receptance. The corresponding modal damping ratios of the wheelset in rotation (as defined in Eq.(2)) are obtained by applying experimental modal analysis to the calculated wheelset receptance using the LMS PolyMAX software, and the participation factors are obtained by solving Eq. (5). It can be seen that the key for Eqs. (4)-(6) to be valid is the accurate determination of the damping ratios. LMS PolyMAX is a long-established and widely used software for experimental modal analysis, able to identify modal parameters including damping ratios accurately. Since here the receptance is computed from a FE model without 'measurement noise', the accuracy in the identified damping ratios can be further assured. Table 2 gives the damping ratios of the wheelset obtained when it is not in rotation and when it travels at 200 km/h or 400 km/h. The results in this section are produced based on the driving point receptance of the rotating wheelset at the wheel-rail contact point. In Table 2, the first column, m, defines the number of nodal diameters (or circumferential order) of the mode of the wheelset not in rotation.

When the wheelset is not in rotation, the damping ratios should all be equal to 0.001, since a constant damping loss factor of 0.002 has been given for the calculation of the receptance. It can be seen from the third column of Table 2, the EMA software can accurately recover the damping ratios. When the wheelset is in rotation, each non-rotating natural frequency is split into two resonance frequencies (except for the mode at 3291 Hz which is at the 0th circumferential order), one lower and the other higher than the natural frequency. The difference between these two resonance frequencies is given in brackets and can be seen to be smaller than $2m$ times the wheel rotation speed (20.5 Hz for 200 km/h and 41 Hz for 400 km/h). The resulting damping ratios are still around 0.001; however, it is evident that the one associated with the lower frequency of each pair is increased from the non-rotational value while that associated with the higher frequency is reduced. These changes generally increase with wheelset rotation speed. The values in brackets are the relative changes in damping ratio from the exact non-rotating value. The largest change in damping ratio at 400 km/h is 19% for the mode originally at 119 Hz (the first bending mode of the wheelset).

Table 2 Modal damping ratios of the wheelset

m	Natural Freq. (Hz) (0 km/h)	Damping ratio (%) (0 km/h)	Resonance Freq. (Hz) (200 km/h)	Damping ratio (%) (200 km/h)	Resonance Freq. (Hz) (400 km/h)	Damping ratio (%) (400 km/h)
1	119	0.100	105.5	0.110 (+10%)	92	0.119 (+19%)
			132.5 (27)	0.090 (-10%)	146 (54)	0.081 (-19%)
1	351.5	0.100	345	0.102 (+2%)	340	0.102 (+2%)
			359.5 (14.5)	0.098 (-2%)	369 (29)	0.095 (-5%)
1	899.5	0.101	897.5	0.100 (+0%)	895.5	0.100 (+0%)
			902 (4.5)	0.100 (-0%)	905 (9.5)	0.099 (-1%)
1	1504	0.100	1498	0.100 (+0%)	1492	0.101 (+1%)
			1509 (11)	0.100 (-0%)	1515 (23)	0.099 (-1%)
2	2154	0.102	2130	0.102 (+2%)	2107	0.103 (+3%)
			2177 (47)	0.098 (-2%)	2201 (94)	0.096 (-4%)
2	2515	0.094	2474	0.102 (+2%)	2434	0.105 (+5%)
			2555 (81)	0.099 (-1%)	2596 (162)	0.096 (-4%)
3	2825	0.107	2776	0.099 (-1%)	2727	0.103 (+3%)
			2874 (98)	0.095 (-5%)	2922 (195)	0.097 (-3%)
0	3291	0.100	3292	0.098 (-2%)	3292	0.101 (+1%)
4	3547	0.099	3473	0.102 (+2%)	3401	0.104 (+4%)
			3619 (146)	0.098 (-2%)	3692 (291)	0.096 (-4%)
1	3797	0.101	3774	0.101 (+1%)	3752	0.102 (+2%)
			3821 (47)	0.100 (-0%)	3844 (92)	0.099 (-1%)

Fig. 8 shows the real and imaginary parts of the vertical receptance (excluding the rigid body part) from the FE simulation and from the reconstruction for a wheel speed of 400 km/h. It can be seen that the simulated and reconstructed curves almost overlap each other, especially around the resonances, confirming the accuracy of the EMA-identified modal parameters. In Fig. 8(b) there are some differences in the imaginary part in the region between resonances below 2000 Hz. They may be due to the approximation of the receptance of the rotating wheelset by that of a stationary elasticity via Eq. (2).

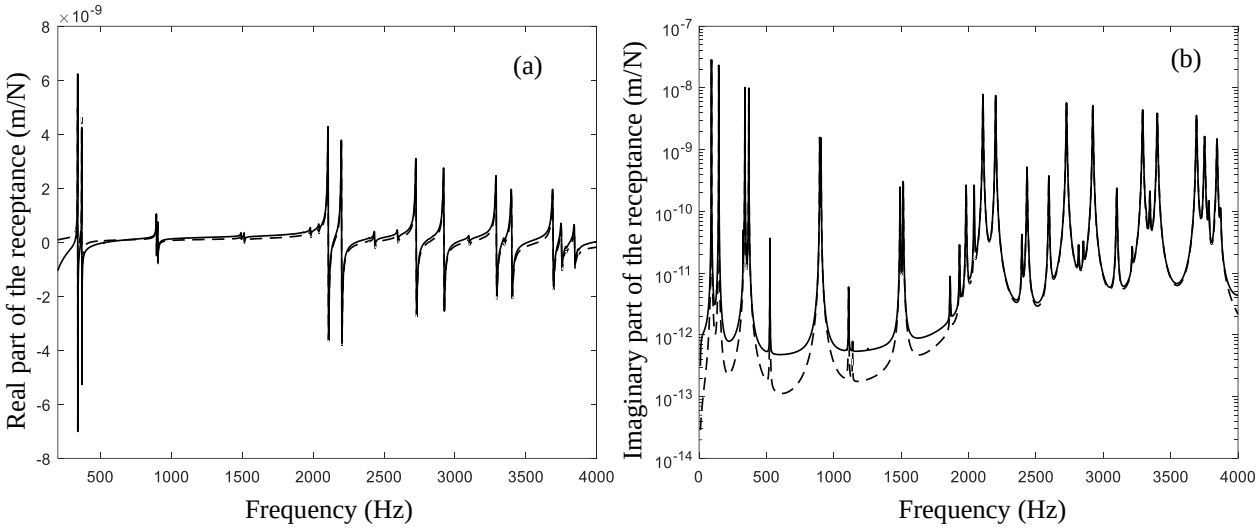

Fig. 8. The vertical receptance (excluding the rigid body part) of the wheelset at the wheel-rail contact point. (a) Real part; (b) imaginary part (shown positive for clarity). ——, FE-calculated; − − −, from Eq. (2). The wheelset rotates at 400 km/h.

Fig. 9 shows the time-domain Green's function of the wheelset (excluding the rigid body part) not in rotation, and rotating at 200km/h and 400 km/h, for a time interval of 0 to 2 s (Fig. 9(a)). Due to the low damping, the Green's function decays very slowly. From Fig. 9(b) it can be seen that in the early stage (about 0 to 2 ms for 200 km/h and 0 to 1 ms for 400 km/h) after the impact, the response of the wheelset not in rotation and that in rotation are almost identical. Thus, for this short period, the effect of wheelset rotation can be considered negligible, suggesting that wheel rotation may have a negligible effect on wheel-rail impact, see Section 4 below. After this initial period, however, differences due to wheelset rotation become apparent. Since all the damping ratios are nearly the same, the high frequency components in the Green's function die out quickly, leaving those at lower frequency. When the wheelset is not rotating, only the first component remains at 119 Hz, exhibiting a sinusoidal pattern (solid line in Fig. 9(c)). However, when the wheelset is rotating, since the lowest non-rotating modal frequency is split into two (see Table 2), the Green's function displays a more complex beating pattern, as shown by the dashed (200 km/h) and dash-dotted (400 km/h) curves in Fig. 9(c).

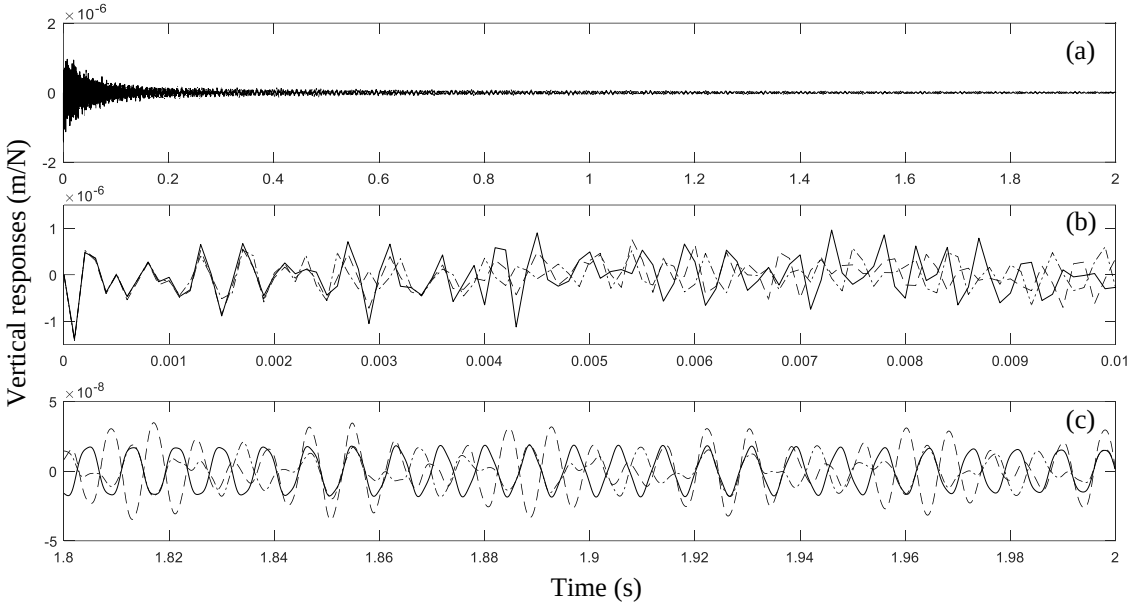

Fig. 9. The time-domain moving Green's function of the wheel (excluding the rigid body part). (a) 0 - 2s; (b) 0 - 0.01s; (c) 1.8 - 2s. ——, wheelset not in rotation; − − −, wheelset rotating at 200 km/h; − · −, wheelset rotating at 400 km/h.

4. Application of the wheelset-rail interaction model for wheel-rail forces

In this section, wheel-rail forces are predicted based on the time-domain moving Green's functions calculated in Section 3. Four excitation cases are considered: (1) parametric excitation only; (2) roughness at a single wavelength; (3) a rail indentation; (4) two wheelsets passing over the rail indentation. For the first three cases, only a single wheelset is considered. For each of the first three cases, both non-rotating and rotating wheelset conditions are considered, but in both cases, the wheelset is assumed to move along the track at 400 km/h. Wheel-rail forces in Cases 2 to 4 are a combined result of wheel-rail irregularity and parametric excitation. In each case, at $t = 0$ the first wheelset is just above a sleeper.

4.1 Wheel-rail interaction purely due to parametric excitation

Fig. 10 shows the wheel-rail force purely due to parametric excitation at 400 km/h. Simulations are carried out for a total of 150 sleeper bays. Fig. 10(a) shows the achieved steady-state wheel-rail force when the wheelset passes between the 130th and 150th sleepers. Fig. 10(b) shows the corresponding frequency spectrum obtained by performing FFT on the signal (the time length is 0.11 s, and therefore the frequency resolution is about 9 Hz. Use of multiple, rather than a single, periods of the wheel-rail force time-history in FFT will lead to a spectrum with a fine frequency resolution). No windowing is

applied as this is a periodic signal (but see below). It should be pointed out that, in theory the wheel-rail force spectrum in Fig. 10(b) should be discrete, having components (the peaks in Fig. 10(b)) at the sleeper-passing frequency and its multiples only. The broadband response between the peaks is a result of the FFT used to calculate the spectrum.

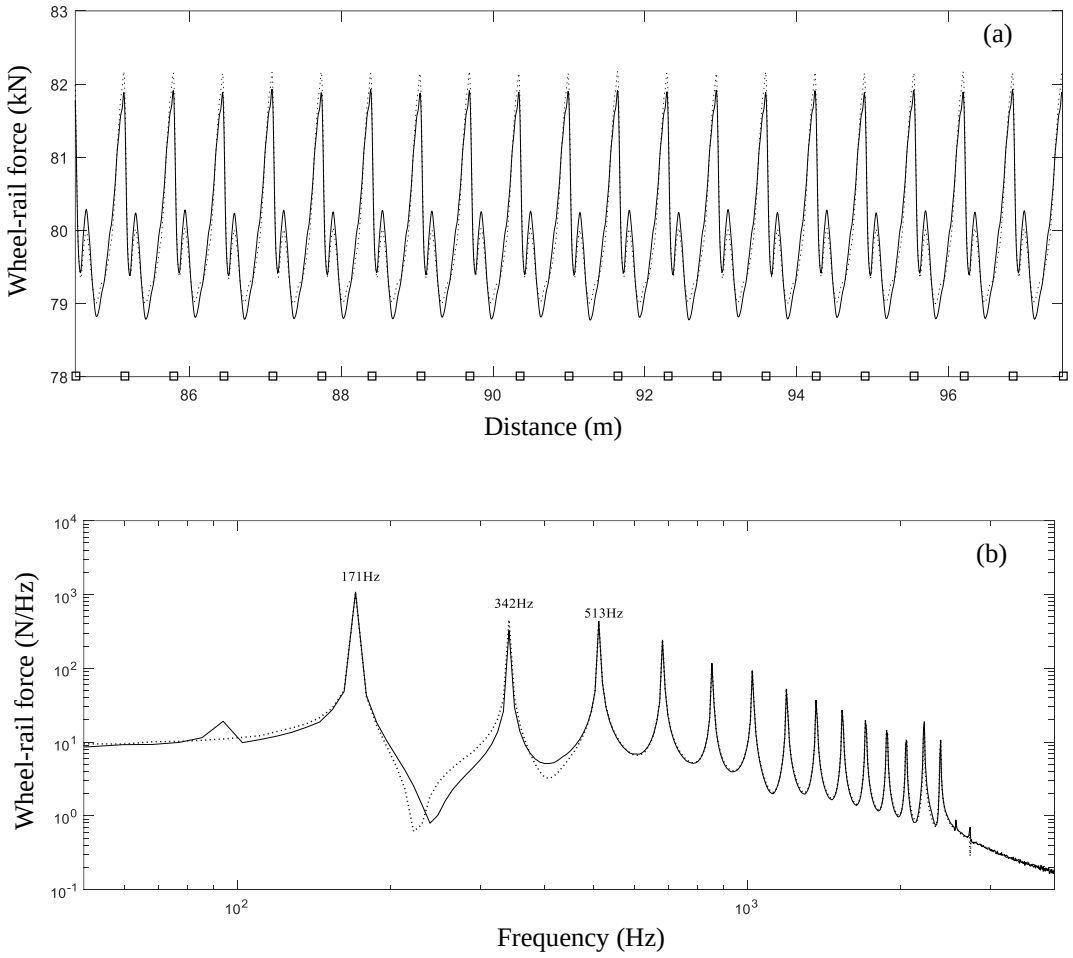

Fig. 10. Wheel-rail force purely due to parametric excitation. (a) wheel-rail force distance-history; (b) wheel-rail force frequency spectrum. ——, rotating wheel; ·····, non-rotating wheel; □ sleeper position. Wheel speed c = 400 km/h.

The contact force reaches its maximum above the sleepers and minimum at mid-span. A local peak also appears before the mid-span position, indicating that the wheel-rail force has a number of important frequency components. In theory, the steady-state wheel-rail force has components only at the sleeper-passing frequency (171 Hz at 400 km/h) and its multiples. The model has correctly predicted this, as evidenced by the evenly spaced peaks from 171 Hz in Fig. 10(b). The first one and the last two peaks, very low compared to other peaks, are due to the transient component remaining in the wheel-rail force time-history used for producing the spectrum.

There are some differences in wheel-rail force between the rotating and non-rotating wheelset in Fig. 10(a). Fig. 10(b) indicates that the difference is mainly at the component of the second order of sleeper-passing at 342 Hz. This may be explained by the fact that inclusion of wheelset rotation makes one of the resonance frequencies of the wheelset (340 Hz, see Table 2) nearly identical to the second order frequency of sleeper-passing (342 Hz) at this speed.

4.2 Wheel-rail interaction due to roughness at a single wavelength

Wheel polygonisation at a particular order (between 17 and 24 [31]) is often observed on China's high-speed trains. Rail corrugation at a particular wavelength may also occur although it is less common on high-speed lines. Both the wheel polygonisation and rail corrugation are equivalent to a periodic wheel-rail roughness at a single wavelength λ, i.e.

$$z(x) = A\cos(2\pi x / \lambda + \varphi_0). \tag{13}$$

where A stands for the amplitude of the roughness, φ_0 is a phase angle, and for the nth order of wheel polygonisation, $\lambda = 2\pi R / n$, where R is the nominal radius of the wheel. Results are shown for two examples corresponding to a typical order of wheel polygonization and a typical wavelength of rail corrugation. Due to the symmetry of the model the same roughness is effectively applied to both the wheel-rail contacts of the wheelset.

4.2.1 Due to a wheel polygonisation

First, the 20th order wheel polygonisation with an amplitude of 0.06 mm (corresponding to an rms amplitude of 32.6 dB re 10^{-6} m) is considered. The corresponding wavelength is 0.135 m and the roughness excitation frequency is about 823 Hz at 400 km/h. As $27 \times 0.65 = 130 \times 0.135 = 17.55$, the roughness can be regarded as periodic with the period being 17.55 m, which is 27 times the period (0.65 m) of the track. Thus, according to Ref. [13], if the contact spring is linearized, the steady-state wheel-rail force distance-history is also periodic with a period of 17.55 m, and has components only at frequencies given by $(k + n/27) f_S$, where f_S denotes the sleeper-passing frequency, $n = 1, 2, \cdots, 26$, and $k = 0, 1, \cdots \infty$. At the roughness excitation frequency, k = 4 and n = 22.

The wheel-rail force is solved for 150 spans (97.5 m, 5.6 times the roughness period), and Fig. 11(a) shows the result plotted against distance between Sleepers 75 and 80 once steady state has been achieved. The results with and without rotation appear almost identical, indicating that the effect of the wheel

rotation can be neglected in this case. This may be explained by the fact that, as indicated in Fig. 4, at the roughness excitation frequency (823 Hz) the receptance of the rail is much higher than that of the wheel and the wheel-rail force is mainly determined by the receptance of the rail. However, a beating pattern in the wheel-rail force is clearly evident corresponding to the sleeper-passing frequency.

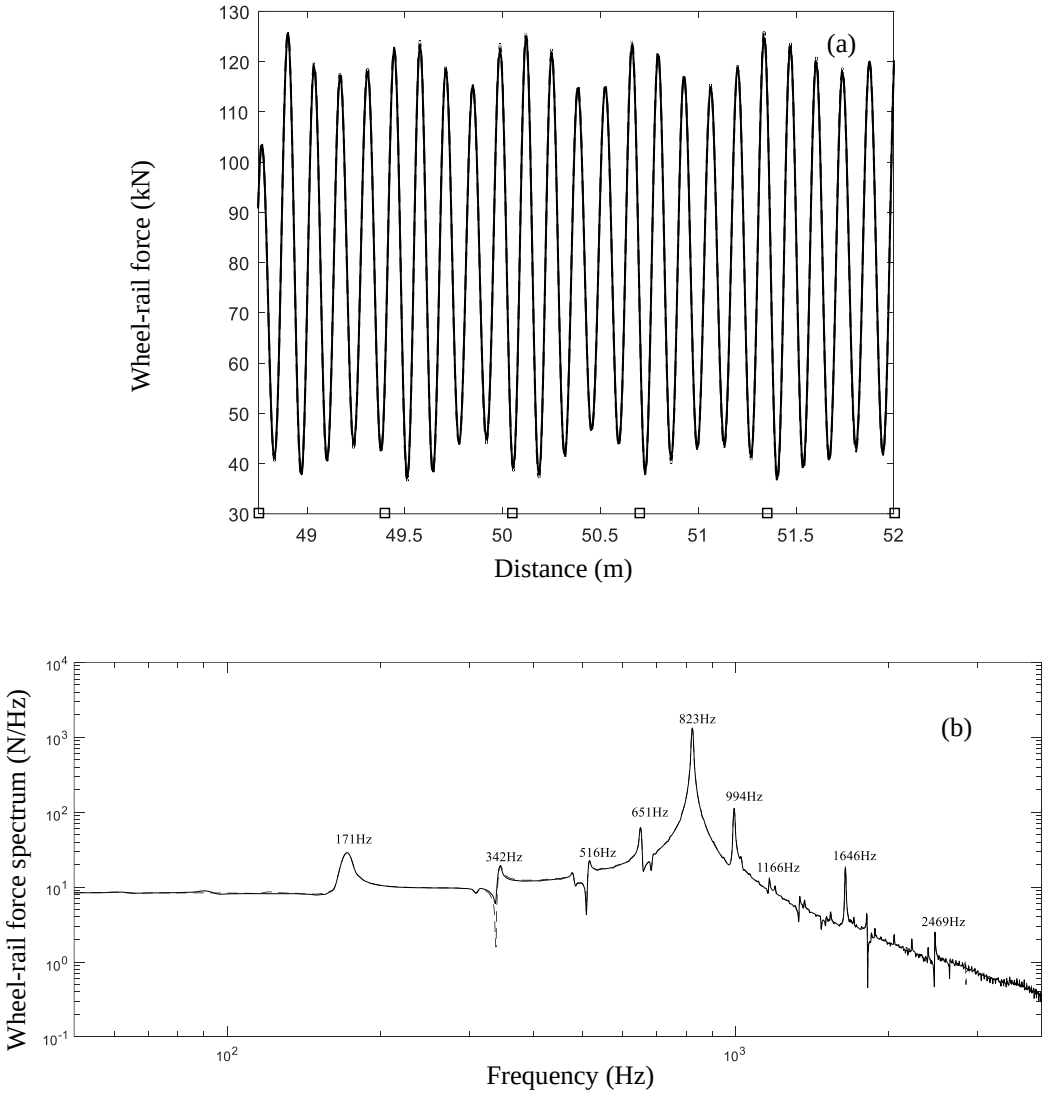

Fig. 11. Wheel-rail force due to wheel polygonisation. (a) Wheel-rail force plotted against position; (b) wheel-rail force frequency spectrum. ——, rotating wheel; − − −, non-rotating wheel; □ sleeper position. Wheel speed c = 400 km/h.

To explore the frequency content, the wheel-rail force frequency spectrum is produced using a Hanning window, with a frequency resolution of 1 Hz. The result is shown in Fig. 11(b). It can be seen that, the highest peak at 823 Hz corresponds to the wheel polygonisation excitation. Smaller peaks also appear at the multiples of this frequency (1646 Hz, 2496 Hz). This is caused by the non-linearity in the

wheel-rail contact. The wheel-rail force has been recalculated with a linearized contact spring (not shown), and the corresponding frequency spectrum is found not to contain the peaks at 1646 Hz and 2496 Hz.

Other peaks are evident in Fig. 11 at 651 Hz, 994 Hz and 1166 Hz. These, and the polygonisation frequency are separated by the sleeper-passing frequency 171 Hz or multiples of it. In other words, if the roughness excitation frequency is denoted by f_P, and the sleeper-passing frequency is denoted by f_S, then peaks may occur at $f_P \pm nf_S$ ($823 \pm n \times 171$ Hz for 400 km/h), where n stands for an integer. This frequency modulation phenomenon is caused by the parametric excitation, which cannot be predicted using the 'moving irregularity' approach. In practice, these frequencies are often mistakenly associated with wheel out-of-round or rail corrugation.

Such frequency modulation is often observed in practice. Fig. 12 shows a spectrum of interior noise measured in a high-speed train above a bogie. The train speed is 300 km/h. The sleeper-passing frequency is about 128 Hz, and the excitation frequency due to the 18th order wheel polygonisation is about 586 Hz. Peaks at 330 Hz, 458 Hz, 586 Hz, 714 Hz and 842 Hz are exactly separated by the sleeper-passing frequency, showing a similar phenomenon to the result in Fig. 11.

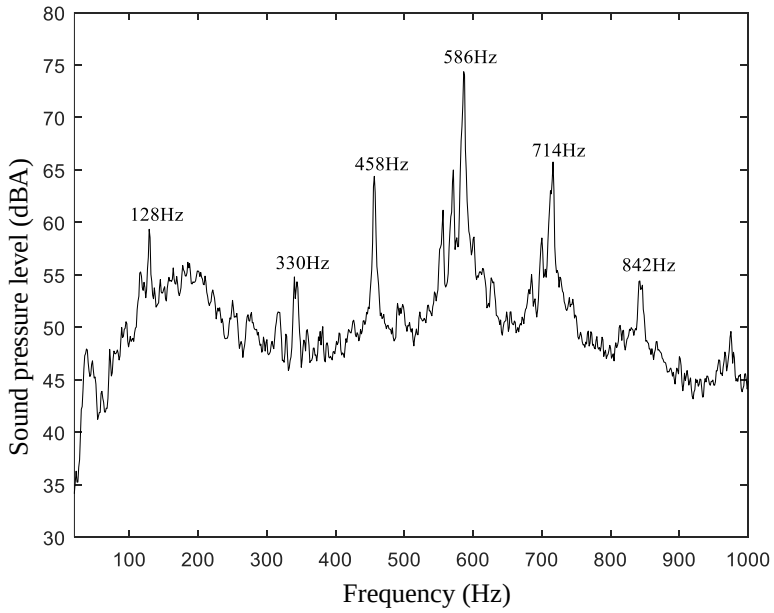

Fig. 12. Measured interior noise in a high-speed train above a bogie. The train speed is 300 km/h.

4.2.2 Due to a short-pitch rail corrugation

Second, a short-pitch rail corrugation is applied to the wheel-rail interaction model. Here, the corrugation amplitude is taken to be 0.01 mm and the wavelength is taken to be either 50.5 mm or 51.6 mm. Thus, at 400 km/h, the roughness excitation frequency is 2201 Hz, which is the same as one of the resonance frequencies of the rotating wheelset, or 2154 Hz, the resonance frequency of the non-rotating wheelset (Table 2). Around these two frequencies, the wheelset is more flexible than the rail (see Fig. 4).

For the corrugation of wavelength 50.5 mm, the roughness can be regarded as periodic with a period of 65.65 m which is 101 times the period of the track ($101\times 0.65 = 1300\times 0.0505 = 65.65$). Thus, according to Ref. [13], if the contact spring is linearized, the steady-state wheel-rail force is also periodic with the period being 65.65 m, and has components only at frequencies given by $(k + n/101) f_S$, where f_S denotes the sleeper-passing frequency, $n = 1, 2, \cdots, 100$, and $k = 0, 1, \cdots \infty$. For small *n*, the frequencies are close to the sleeper-passing frequency and its multiples. At the roughness excitation frequency, k = 12 and n = 88.

The wheel-rail force is solved for 150 spans (97.5 m, 31.85 m longer than the aforementioned period of the steady-state wheel-rail force) and the result is shown between Sleeper 70 and Sleeper 150 in Fig. 13. The corrugation has been introduced after the steady-state response to the parametric excitation has been achieved. It can be seen that the wheel-rail force due to the corrugation becomes steady after about the position x = 72m (near the 110th sleeper). Therefore, the wheel-rail force between Sleeper 120 and Sleeper 150 (part of which is shown in Fig. 14(a)) is taken for analysis and discussion.

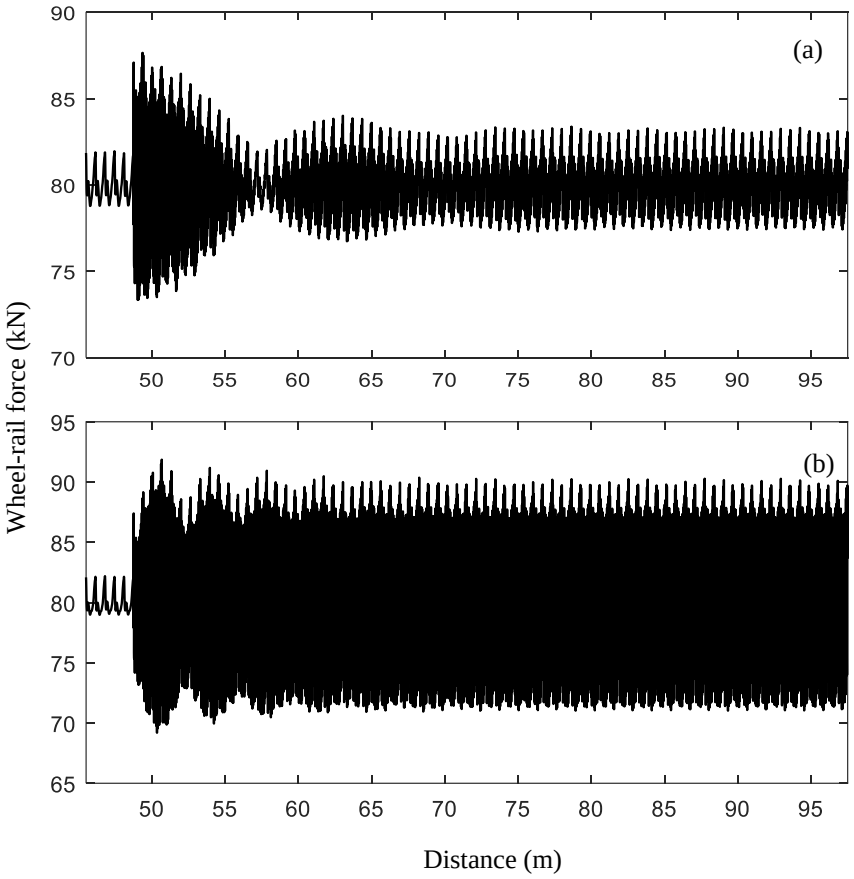

Fig. 13. Wheel-rail force due to rail corrugation with amplitude of 0.01 mm and wavelength of 50.5 mm plotted against position. (a) Rotating wheel; (b) non-rotating wheel. Wheel speed c = 400 km/h.

Fig. 14(a) shows a close-up view of the steady-state wheel-rail force due to the 50.5 mm wavelength rail corrugation plotted against position. The roughness excitation frequency is about 2201 Hz, equal to the resonance frequency of the rotating wheelset. Therefore, at this frequency, the rotating wheelset has a much higher receptance, or equivalently, is much dynamically softer, than the non-rotating wheelset. As a result, fluctuations in the wheel-rail force for the rotating wheelset is much smaller than for the non-rotating wheelset. The corresponding frequency spectra are shown in Fig. 14(b) using a Hanning window with a frequency resolution of 1 Hz (between Sleeper 120 and Sleeper 150). In both cases the highest peak at 2201 Hz corresponds to the rail corrugation excitation. The remaining peaks are the sleeper-passing frequency and its multiples (171 Hz etc.) but there is no obvious modulation of the main peak.

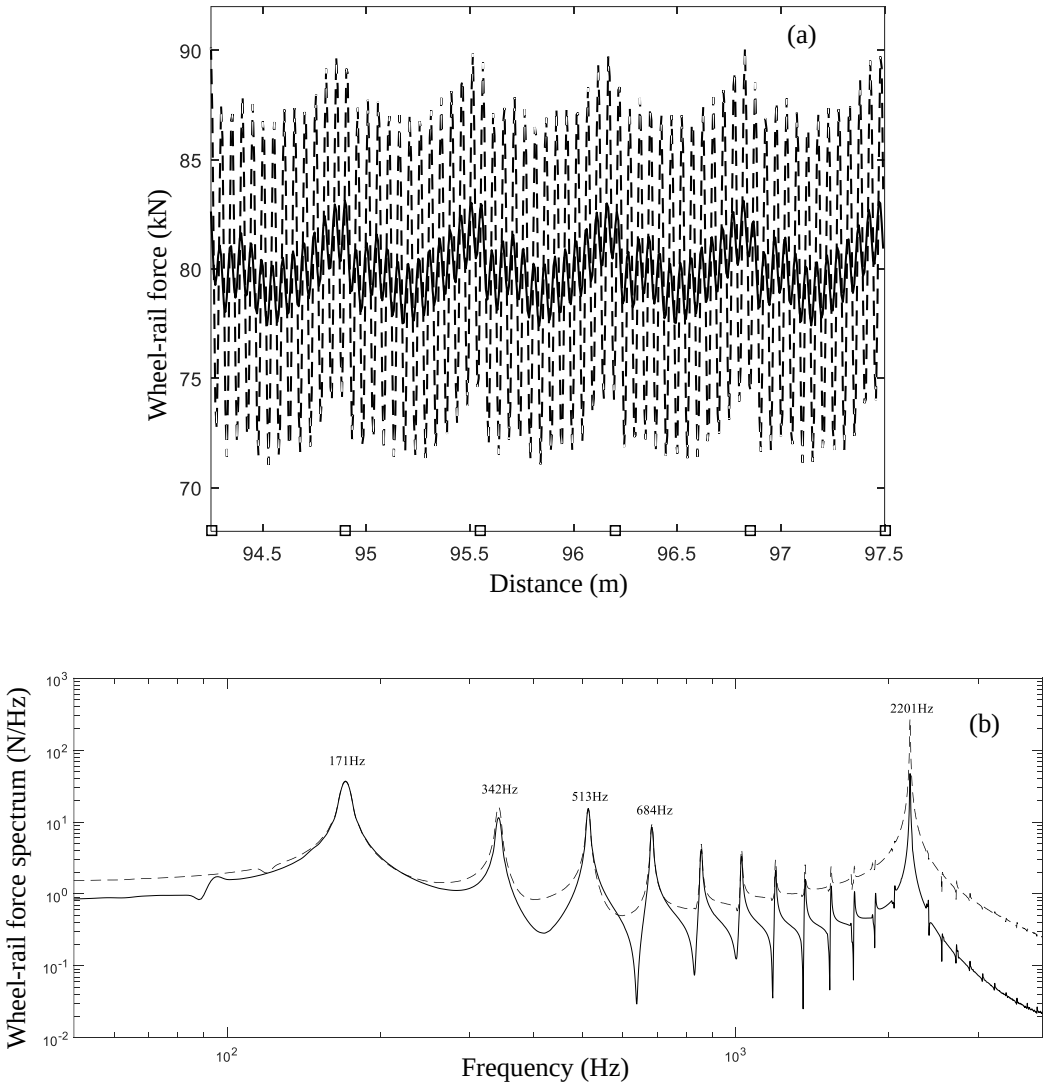

Fig. 14. Wheel-rail force due to rail corrugation with amplitude of 0.01 mm and wavelength of 50.5 mm. (a) Wheel-rail force plotted against position; (b) wheel-rail force frequency spectrum. ——, rotating wheel; − − −, non-rotating wheel; □ sleeper position. Wheel speed c = 400 km/h.

Fig. 15(a) shows the steady-state wheel-rail force due to the 51.6 mm wavelength rail corrugation. The roughness excitation frequency is about 2154 Hz, equal to the resonance frequency of the non-rotating wheelset. Therefore, at this frequency, the non-rotating wheelset is much more flexible than the rotating wheelset, leading to much smaller fluctuations in the wheel-rail force for the former than for the latter. The corresponding wheel-rail force frequency spectrum is shown in Fig. 15(b). The highest peak occurs at the roughness excitation frequency of 2154 Hz. The other peaks are the sleeper-passing frequency and its multiples (171 Hz etc.).

It is noticed that Fig. 14(b) and Fig. 15(b) do not show evident frequency modulation of the main peak, i.e. peaks at frequencies satisfying $f_P \pm nf_S$. Unlike the results in Fig. 11(b), the roughness frequency considered here is too high for the parametric excitation to have a significant effect on the wheel-rail force due to the roughness excitation. In other words, the wheel-rail force spectrum at and around the roughness excitation frequency may be determined by assuming a free rail, and the actual wheel-rail force spectrum can be approximated by the sum of that spectrum and the one purely due to parametric excitation.

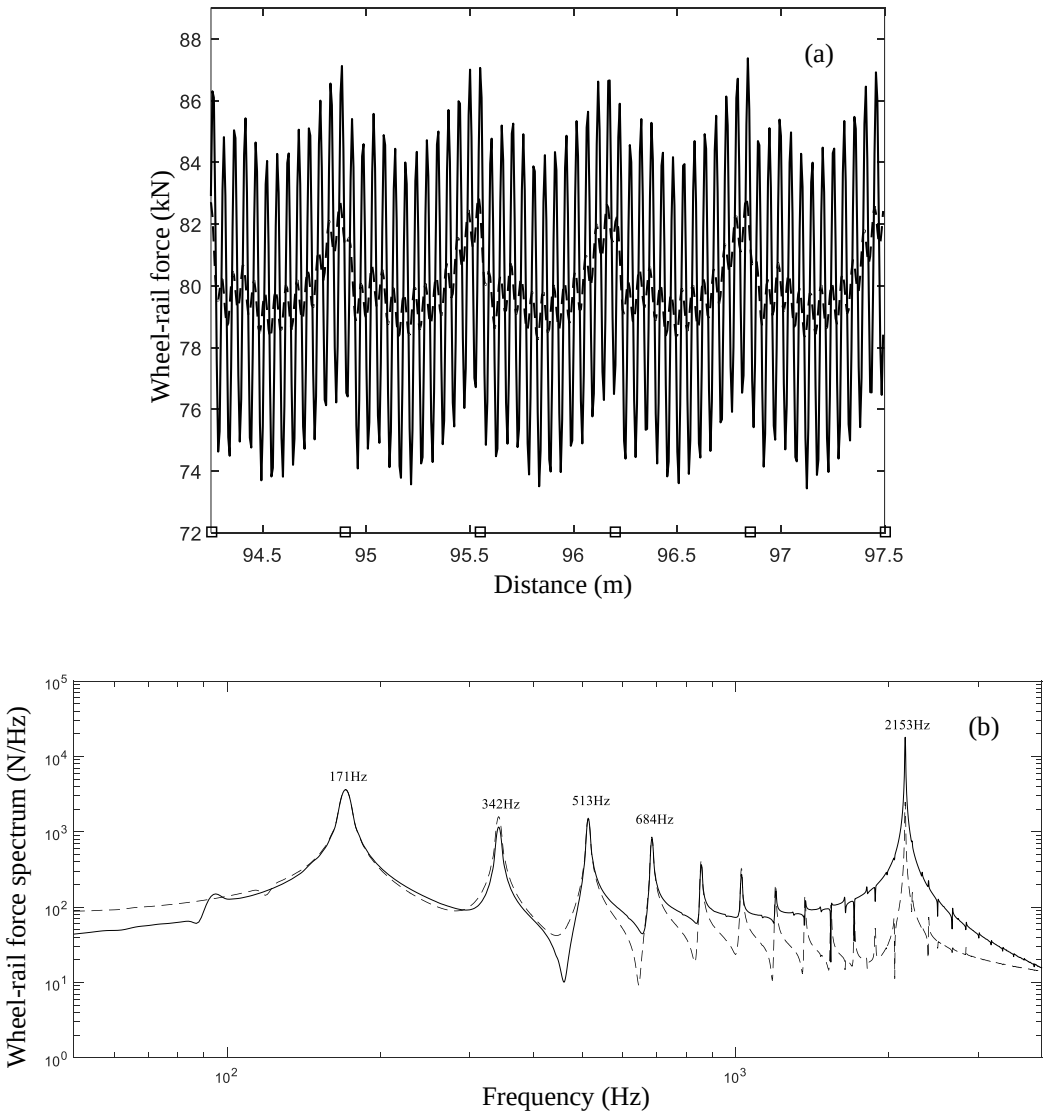

Fig. 15. Wheel-rail force due to rail corrugation with amplitude of 0.01 mm and wavelength of 51.6mm. (a) Wheel-rail force plotted against position; (b) wheel-rail force frequency spectrum. ——, rotating wheel; – – –, non-rotating wheel; □ sleeper position. Wheel speed c = 400 km/h.

4.3 Wheel-rail interaction due to a rail indentation

In this section, a rail indentation is applied to the wheel-rail interaction model. The indentation is described by

$$z(x) = -\frac{e}{2}(1-\cos\frac{2\pi x}{l}), (0 \le x \le l) \quad . (14)$$

where e = 0.35 mm stands for the depth of the indentation and l = 60 mm stands for its length. In this section, the wheel-rail force is simulated for 150 spans. The rail indentation is located at the mid-span between the 75th and 76th sleeper and, due to the symmetry of the model, is applied to both rails. The wheelset and track responses due to parametric interaction are already in a steady state when the wheelset arrives at the indentation.

The predicted wheel-rail force is plotted in Fig. 16(a) against position. It can be seen that the effect of wheel rotation on the wheel-rail impact force is negligible. Differences are seen only well after the impact. Due to the depth of the indentation, loss of contact occurs.

Fig. 16(b) presents the corresponding frequency spectra using an exponential window with a total decay of 20 dB for a duration of 0.5 s. The frequency resolution is 2 Hz. A number of peaks appear in the spectra. The peak at about 68 Hz is the P2 frequency. The sleeper-passing frequency (171 Hz) and its multiples (342, 513, 684, 854, 1196, 1368, 1537, 1710, 1880 Hz etc.) are clearly seen.

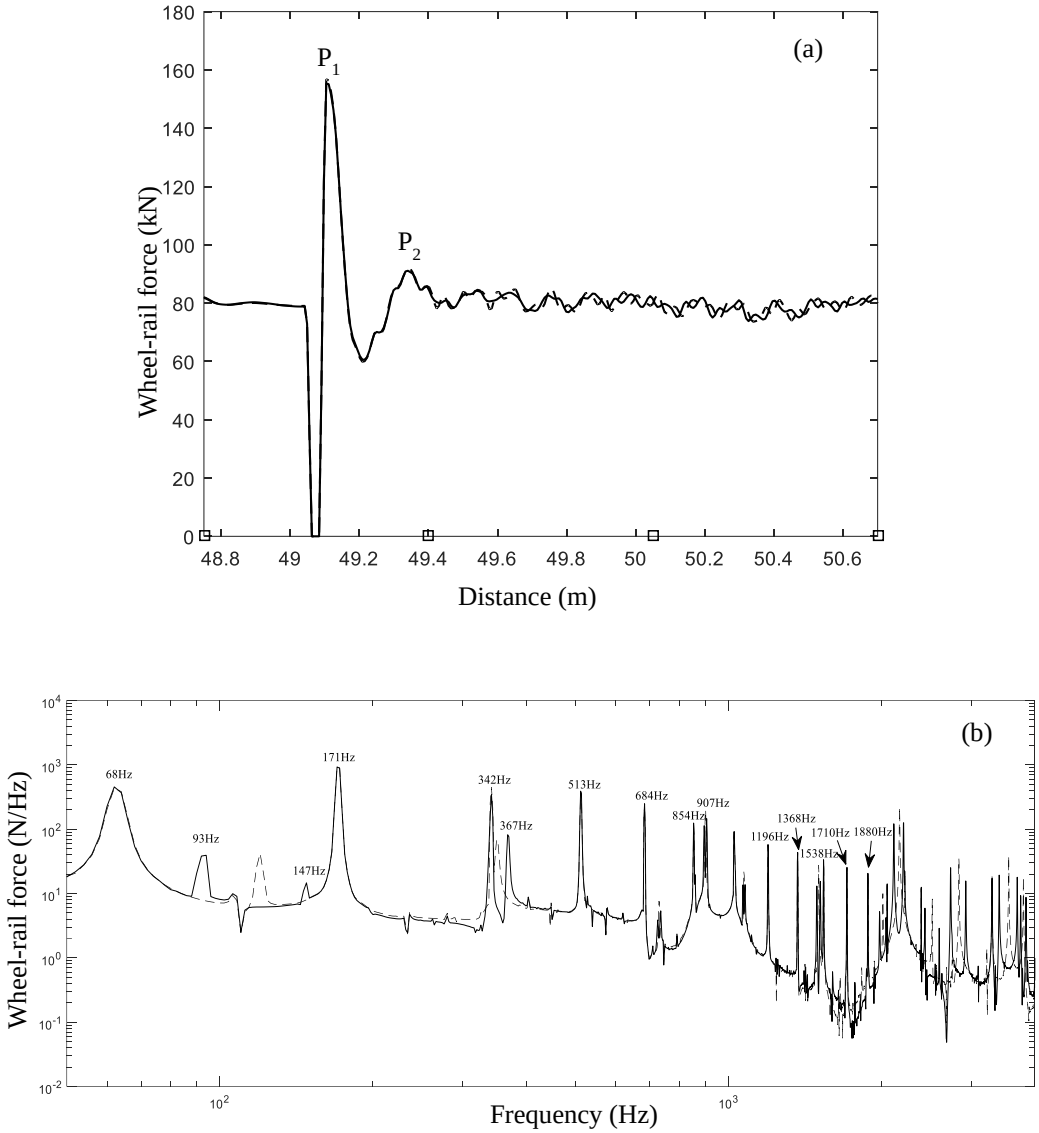

Fig. 16. Wheel-rail force due to a rail indentation. (a) Wheel-rail force distance-history; (b) wheel-rail force frequency spectra. ——, rotating wheel; − − −, non-rotating wheel; □ sleeper position. Wheel speed c = 400 km/h.

The smallest singular value of the coefficient matrix of Eq.(12) is shown in Fig. 17 in comparison with the receptance of the rail (for stationary load) and that of the wheelset rotating at 400 km/h. Dip frequencies of 68 Hz, 93 Hz, 147 Hz, 337 Hz, 367 Hz and 907 Hz are indicated in the figure. They are the characteristic frequencies of the wheelset-track system. As shown in Fig. 16, in addition to the sleeper-passing frequency and its multiples, the wheel-rail force also exhibits a peak at these characteristic frequencies (except for 337 Hz and this may be due to that it is too close to the second order sleeper-passing frequency at 342 Hz). When frequency is higher than 2000 Hz, the peaks are all

related to the dip frequencies shown in Fig. 17. Since now the track is much stiffer than the wheelset, these frequencies are essentially the anti-resonance frequencies of the wheelset.

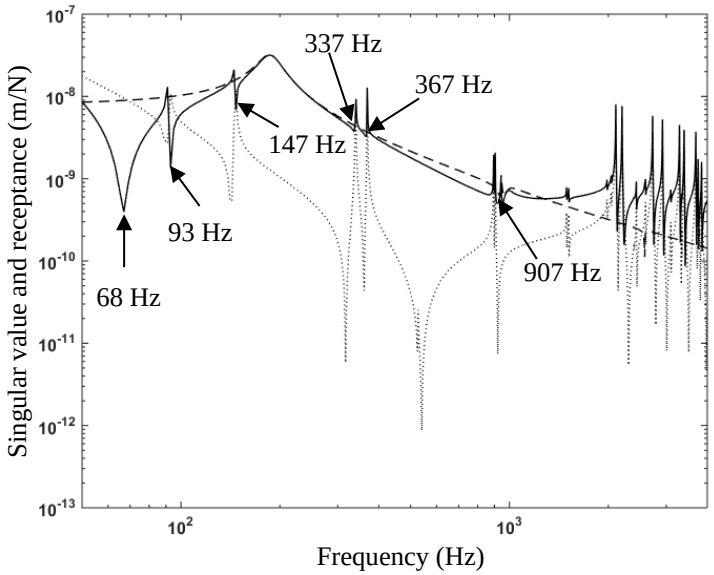

Fig. 17. ——, the singular value of the coefficient matrix of Eq. (12); − − −, the receptance of the rail; ·····, the receptance of the wheelset rotating at 400 km/h.

4.4 Effect of the presence of two wheelsets

In this section, calculations are performed for two identical wheelsets moving and rotating at 400 km/h over the rail indentation defined in Eq. (14). This may serve to simulate wheelset-track interaction for the first (or the last) bogie of which the two wheelsets are well separated from others in a train. At t = 0, the positions of the two wheelsets, according to the dimensions of the bogie, are at 0 m and -2.5 m and the rail indentation is located at the mid-span between the 75th and 76th sleeper relative to the first wheelset. Wheel-rail forces are evaluated for a time duration in which the wheels roll over 97.5 m, or 150 sleeper bays. During that time, both the wheelsets will impact the indentation.

The wheel-rail forces are shown against position in Fig. 18. As each wheelset impacts the indentation, the maximum wheel-rail impact force is similar to the result obtained with a single wheelset (see Fig. 16(a)). However, the impact causes the other wheelset, through wheel-rail interaction, to experience a second, but much smaller, impact. The second impact experienced by the rear wheelset is greater than that by the front wheelset. This is due to the movement of the wheelsets. As a wheelset hits the indentation, an impulsive wave is generated and propagates forward and backward to cause the other

wheelset to experience the second impact. Since the wheelsets move forward, the time for the rear wheelset to receive the backward impulsive wave generated by the front wheelset is shorter (therefore the wave is less attenuated) than that for the front wheelset to receive the forward impulsive wave generated by the rear wheelset.

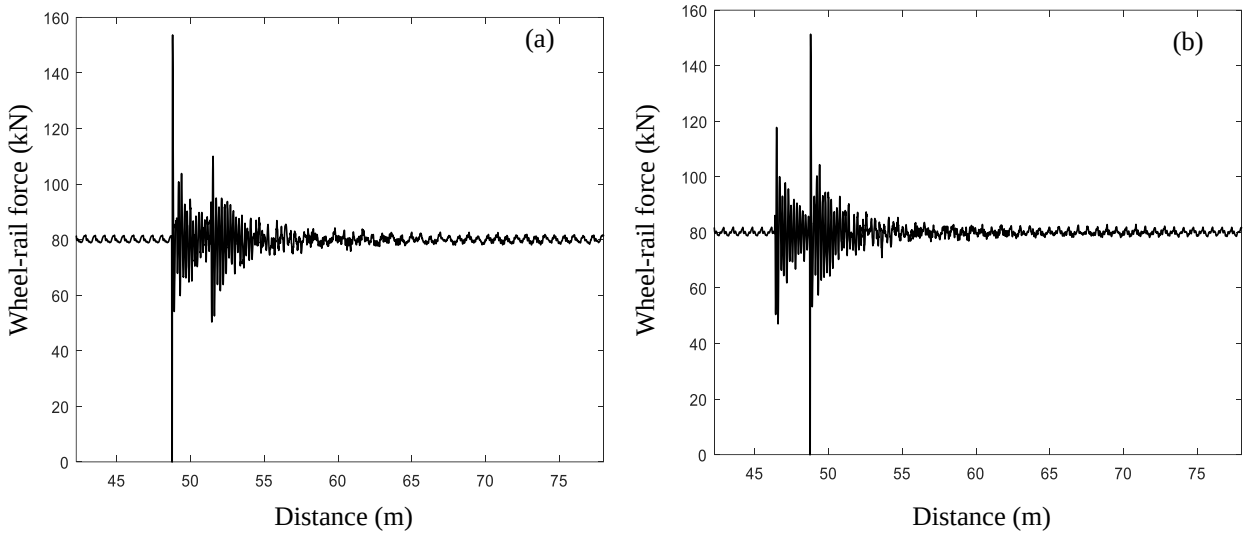

Fig. 18. Wheel-rail force plotted against position for two wheelsets rolling along the rail with an indentation. (a) At the front wheelset; (b) at the rear wheelset. Wheel speed c = 400 km/h.

Fig. 19 presents the corresponding frequency spectra obtained by performing the same procedure as in Section 4.3. The peaks in the spectra of the two wheelsets spectra are similar to those for a single wheelset. A number of peaks can be observed, including the P2 resonance (68 Hz), the sleeper-passing frequency and its multiples (171, 342, 513, 684, 854, 1196, 1368, 1537, 1710 Hz etc.). The amplitudes of some of the peak frequencies are different, probably due to wave reflections in the rail.

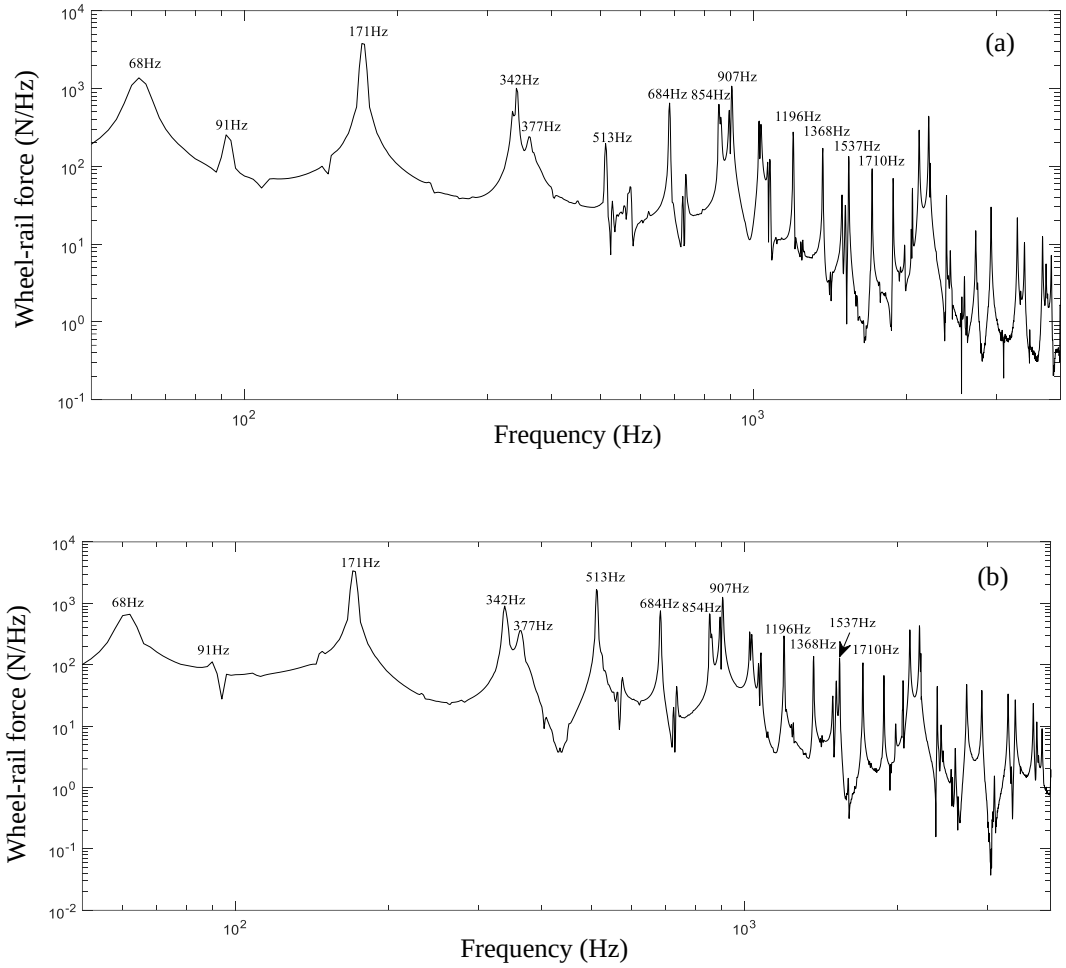

Fig. 19. Wheel-rail force frequency spectrum due to two wheelsets rolling along the rail having a rail indentation. (a) At the front wheelset; (b) at the rear wheelset. Wheel speed c = 400 km/h.

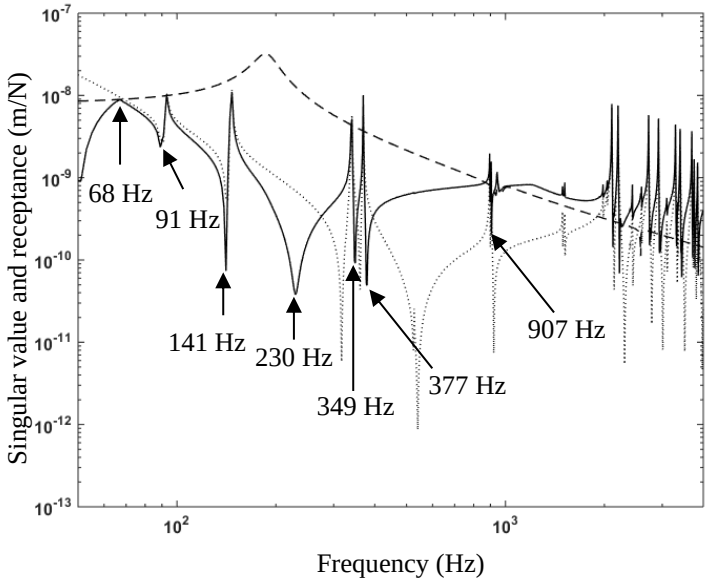

Fig. 20. ——, the singular value of the coefficient matrix of Eq. (12); − − −, the receptance of the rail; ·····, the receptance of the wheelset rotating at 400 km/h.

The smallest singular value of the coefficient matrix of Eq. (12) is shown in Fig. 20 in comparison with the receptance of the rail (for stationary load) and that of the wheelset rotating at 400 km/h. Dip frequencies of 91 Hz, 141 Hz, 230 Hz, 349 Hz, 377 Hz and 907 Hz are indicated in the figure. Compared with the single wheelset case (Fig. 17), the dip at 68 Hz now becomes a broad peak. However, a peak still appears to the wheel-rail force at this frequency. There is a new dip at 230 Hz, however, this characteristic frequency is not excited by the impacts. In summary, in terms of wheel-rail force, the sleeper-passing frequency is more important than the characteristic frequencies (except for the one at 907 Hz) of the wheelset-track system.

5. Conclusions

In this paper, the method based on time-domain moving Green's functions is extended and employed to calculate wheel-rail forces for a single, or multiple, wheelsets rolling over a track; the track is considered as an infinitely long periodic structure. The flexibility and rotation of the wheelset are taken into account by incorporating the associated time-domain moving Green's function of the wheelset. These are derived from the corresponding receptance by applying an experimental modal analysis technique. To reveal the frequency content of high-speed wheel-rail interaction, wheel-rail forces are calculated for a set of parameters typical of the Chinese high-speed railway (a non-ballast slab track) and for a number of typical excitation cases, including purely parametric excitation, wheel polygonisation,

rail corrugation and rail indentation. Effects of wheel rotation on wheel-rail force are studied and, comparisons are made between a single wheelset and multiple wheelsets. The main conclusions can be summarised as follow:

Wheelset rotation can be neglected for purely parametric excitation and for discrete wheel/rail irregularities. For roughness at a single wavelength (e.g. wheel polygonisation or rail corrugation), if the rail receptance is dominant over that of the wheel, then the effect of wheel rotation can be neglected; however, if the wheel receptance is dominant over those of the rail and the contact spring, then the effect of wheel rotation cannot be neglected. This is especially true when the roughness excitation frequency is close to a resonance frequency of the wheelset, either in rotation or not.

For roughness at a single wavelength (e.g. wheel polygonisation or rail corrugation), significant frequency modulation may occur in which there are distinct and equally separated peaks around the major roughness excitation frequency. The separation of two neighbouring peaks is equal to the sleeper passing frequency.

Wheel-rail forces purely due to parametric excitation have frequency components only at the sleeper passing frequency and its multiples. The P2 frequency can be excited if there is a transient event (e.g. wheel-rail impact) occurring to the wheel-rail system or if the roughness wavelength corresponds to this frequency. It does not appear in the response to parametric excitation in steady-state wheel-rail interaction.

When a single wheelset impacts a rail indentation, the resulting wheel-rail force contains frequency components at the P2 frequency, sleeper-passing frequency and its multiples, at frequencies (the characteristic frequencies of the wheelset-track system) where the receptances of the wheel and rail cancel each other, and at high anti-resonance frequencies of the wheelset (at these frequencies the rail is much stiffer than the wheelset). When two wheelsets are included, characteristic frequencies of the wheelset-track system change. However, the force spectrum shows similar frequency components compared with a single wheelset, but due to the wave reflections in the rail, the amplitudes of some of these frequencies are different. Although most of the characteristic frequencies of the wheelset-track system may be excited by the impacts, all but the one at 907 Hz are, in terms of wheel-rail force, less important than the sleeper-passing frequency.

Conflict of interest statement

We, the authors of this paper, certify that we have no affiliation with, or involvement in, any organisation or entity with any financial interest, or nonfinancial interest in the subject matter or materials discussed in this manuscript.

Acknowledgement

This work is funded by the National Key R&D Program of China (2016YFE0205200), the National Natural Science Foundation of China (U1834201).

References

[1] K. Knothe, S. L. Grassie, Modelling of railway track and vehicle/track interaction at high frequencies, *Vehicle System Dynamics* 22 (1993) 209-262.

[2] P. J. Remington, Wheel/rail rolling noise, I: Theoretical analysis, *Journal of the Acoustical Society of America* 81 (1987) 1805-1823.

[3] D. J. Thompson, Wheel–rail noise generation, part III: rail vibration, *Journal of Sound and Vibration* 161 (1993) 421–446.

[4] S. L. Grassie, R. W. Gregory, D. Harrison, K. L. Johnson, The dynamic response of railway track to high frequency vertical excitation, *Journal of Mechanical Engineering Science* 24 (1982) 77-90.

[5] T. X. Wu, D. J. Thompson, Application of a multiple-beam model for lateral vibration analysis of a discretely supported rail at high frequencies, *The Journal of the Acoustical Society of America* 108 (2000) 1341-1344.

[6] X. Zhang, D. J. Thompson, Q. Li, D. Kostovasilis, M. G. R. Toward, G. Squicciarini, J. Ryue, A model of a discretely supported railway track based on a 2.5D finite element approach, *Journal of Sound and Vibration* 438 (2019) 153-174.

[7] R. A. Clark, P. A. Dean, J. A. Elkins, et al, An investigation into the dynamic effects of railway vehicles running on corrugated rails, *Journal of Mechanical Engineering Science* 24 (1982) 65-76.

[8] J. C. O. Nielsen, A. Igeland, Vertical dynamic interaction between train and track-influence of wheel and track imperfections, *Journal of Sound and Vibration* 185 (1995) 825–839.

[9] J. Yang, D. J. Thompson, Time-domain prediction of impact noise from wheel flats based on measured profiles, *Journal of Sound and Vibration* 333 (2014) 3981-3995.

[10] L. Ling, X. B. Xiao, J. Y. Xiong, L. Zhou, Z. F. Wen, X. S. Jin, A three-dimensional model for coupling dynamics analysis of high speed train-track system, *Journal of Zhejiang University-SCIENCE A* (*Applied Physics Engineering*) 15 (2014) 964–983.

[11] P. M. Belotserkovskii, The interaction of an infinite wheel-train with a constant spacing between the wheels moving uniformly over a rail track, *Journal of Applied Mathematics and Mechanics* 68 (2004) 923-931.

[12] X. Sheng, C. J. C. Jones, D. J. Thompson, Responses of infinite periodic structures to moving or stationary harmonic loads, *Journal of Sound and Vibration* 282 (2005) 125-149.

[13] X. Sheng, M. Li, C. J. C. Jones, D. J. Thompson, Using the Fourier-series approach to study interactions between moving wheels and a periodically supported rail, *Journal of Sound and Vibration* 303 (2007) 873-894.

[14] X. Sheng, Generalization of the Fourier transform-based method for calculating the response of a periodic railway track subject to a moving harmonic load, *Journal of Modern Transportation* 23 (2015) 12-29.

[15] A. Pieringer, W. Kropp, J. C. O. Nielsen, A time domain model for wheel/rail interaction aiming to include non-linear contact stiffness and tangential friction, *Notes on Numerical Fluid Mechanics and Multidisciplinary Design* 99 (2008) 285-291.

[16] T. Mazilu, Green's functions for analysis of dynamic response of wheel/rail to vertical excitation, *Journal of Sound and Vibration* 306 (2007) 31–58.

[17] T. Mazilu, M. Dumitriu, C. Tudorache, On the dynamic effect between a moving mass and an infinite one-dimensional elastic structure at the stability limit, *Journal of Sound and Vibration* 330 (2011) 3729–3743.

[18] T. Mazilu, M. Dumitriu, C. Tudorache, et al, Using the Green's functions method to study wheelset/ballasted track vertical interaction, *Mathematical and Computer Modelling* 54 (2011) 261-279.

[19] T. Mazilu, Interaction between moving tandem wheels and an infinite rail with periodic supports – Green's matrices of the track method in stationary reference frame, *Journal of Sound and Vibration* 401 (2017) 233-254.

[20] X. Sheng, X. Xiao, S. Zhang, The time-domain moving Green function of a railway track and its application to wheel–rail interactions, *Journal of Sound and Vibration* 377 (2016) 133-154.

[21] D. J. Thompson, Wheel-rail noise generation, Part V: inclusion of wheel rotation, *Journal of Sound and Vibration* 161 (1993) 467-482.

[22] D. J. Thompson, Railway Noise and Vibration: Mechanisms, Modelling and Means, Elsevier, 2009.

[23] J. Fayos, L. Baeza, F. D. Denia, J. E. Tarancón, An Eulerian coordinate-based method for analysing the structural vibrations of a solid of revolution rotating about its main axis, *Journal of Sound and Vibration* 306 (2007) 618–635.

[24] L. Baeza, P. Vila, G. Xie, S. D. Iwnicki, Prediction of rail corrugation using a rotating flexible wheelset coupled with a flexible track model and a non-Hertzian/non-steady contact model, *Journal of Sound and Vibration* 330 (2011) 4493–4507.

[25] J. Giner-Navarro, J. Martínez-Casas, F. D. Denia, L. Baeza, Study of railway curve squeal in the time domain using a high-frequency vehicle/track interaction model, *Journal of Sound and Vibration* 431 (2018) 177-191.

[26] X. Sheng, Y. Liu, X. Zhou, The response of a high-speed train wheel to a harmonic wheel-rail force, *Journal of Physics: Conference Series* 744 (2006) 012145.

[27] L. Baeza, J. Giner-Navarro, D. J. Thompson, J. Monterde, Eulerian models of the rotating flexible wheelset for high frequency railway dynamics, *Journal of Sound and Vibration* 449 (2019) 300-314.

[28] X. Sheng, G. Cheng, Y. He, Modelling the dynamics of a rotating train wheelset, Submitted to Chinese Journal of Mechanical Engineering (2020).

[29] J. C. O. Nielsen, A Johansson, Out-of-round railway wheels-a literature survey, Proceedings of the Institution of Mechanical Engineers, Part F: *Journal of Rail and Rapid Transit* 214 (2000) 79-91.

[30] Y. Wu, X. Du, H. Zhang, et al, Experimental analysis of the mechanism of high-order polygonal wear of wheels of a high-speed train, *Journal of Zhejiang University-SCIENCE A* 18 (2017) 579-592.

[31] X. Wu, S. Rakheja, W. Cai, et al, A study of formation of high order wheel polygonalization, *Wear* 424 (2019) 1-14.

[32] W. Cai, M. Chi, X. Wu, et al, Experimental and numerical analysis of the polygonal wear of high-

speed trains, *Wear* 440 (2019) 203079.

[33] H. Dai, D. Li, S. Zhuang, Study on the mechanism of high order out of round and wear of high-speed railway train's wheel, *Dynamics of Vehicles on Roads and Tracks* 2 (2017) 1321-1327.

[34] X. Sheng, T. Zhong, Y. Li, Vibration and sound radiation of slab high-speed railway tracks subject to a moving harmonic load, *Journal of Sound and Vibration* 395 (2017) 160–186.

[35] D. J. Ewins, Modal Testing: Theory and Practice, Research Studies Press (1984).

[36] V. K. Garg, R.V. Dukkipati, Dynamics of Railway Vehicle Systems, Academic Press, Canada, 1984.

[37] S. H. Crandall, The role of damping in vibration theory, *Journal of Sound and Vibration* 11 (1970) 3–18.

Appendix. Solution of Eq. (11)

It is assumed that the dynamic wheel-rail force appears only for positive time. Thus, at time t_n, where $t_n = n\Delta t$, Δt is the time step and $n = 0,1,2,\cdots$, the displacement of the *k*th wheelset at the wheel-rail contact point can be written as

$$\begin{aligned} w_k^{\mathrm{W}}(t_n) &= \int_{-\infty}^{t_n} \left\{ G_k^{\mathrm{O}}(t_n-\tau)P_{k0} - G_k^{\mathrm{W}}(t_n-\tau)[P_{k0}+f_k(\tau)] \right\} \mathrm{d}\tau \\ &= \int_{-\infty}^{t_n} [G_k^{\mathrm{O}}(t_n-\tau) - G_k^{\mathrm{W}}(t_n-\tau)]P_{k0}\mathrm{d}\tau - \int_{0}^{t_n} G_k^{\mathrm{W}}(t_n-\tau)\, f_k(\tau)\mathrm{d}\tau , \\ &= w_{k0}^{\mathrm{W}}(t_n) - \sum_{i=1}^{n}\int_{t_{i-1}}^{t_i} G_k^{\mathrm{W}}(t_n-\tau)\, f_k(\tau)\mathrm{d}\tau \end{aligned} \tag{A.1}$$

where

$$\begin{aligned} w_{k0}^{\mathrm{W}}(t_n) &= \int_{-\infty}^{t_n} [G_k^{\mathrm{O}}(t_n-\tau) - G_k^{\mathrm{W}}(t_n-\tau)]P_{k0}\mathrm{d}\tau \\ &= \int_{-\infty}^{0} [G_k^{\mathrm{O}}(t_n-\tau) - G_k^{\mathrm{W}}(t_n-\tau)]P_{k0}\mathrm{d}\tau + \int_{0}^{t_n} [G_k^{\mathrm{O}}(t_n-\tau) - G_k^{\mathrm{W}}(t_n-\tau)]P_{k0}\mathrm{d}\tau \\ &= \int_{0}^{\infty} [G_k^{\mathrm{O}}(t_n+\tau) - G_k^{\mathrm{W}}(t_n+\tau)]P_{k0}\mathrm{d}\tau + \int_{0}^{t_n} [G_k^{\mathrm{O}}(t_n-\tau) - G_k^{\mathrm{W}}(t_n-\tau)]P_{k0}\mathrm{d}\tau \\ &= \sum_{i=1}^{I}\int_{t_{i-1}}^{t_i} [G_k^{\mathrm{O}}(t_n+\tau) - G_k^{\mathrm{W}}(t_n+\tau)]P_{k0}\mathrm{d}\tau + \sum_{i=1}^{n}\int_{t_{i-1}}^{t_i} [G_k^{\mathrm{O}}(t_n-\tau) - G_k^{\mathrm{W}}(t_n-\tau)]P_{k0}\mathrm{d}\tau \end{aligned} . \tag{A.2}$$

In Eq. (A.2), I is an integer large enough for the truncation made for the first integral in Eq. (A.2) to be valid.

Since the interval $[t_{i-1}, t_i]$ is small, the functions appearing in the integrals in Eq. (A.1) can be linearized for that interval (in other words, the choice of the time step Δt must be such that the linearization is sufficiently accurate), giving

$$\begin{aligned} w_k^{\mathrm{W}}(t_n) &= w_{k0}^{\mathrm{W}}(t_n) - \sum_{i=1}^{n} \int_{t_{i-1}}^{t_i} G_k^{\mathrm{W}}(t_n - \tau) f_k(\tau) \mathrm{d}\tau \\ &= w_{k0}^{\mathrm{W}}(t_n) - \\ &\quad \Delta t \sum_{i=1}^{n} \left\{ \frac{G_k^{\mathrm{W}}(t_n - t_{i-1}) f_k(t_i) + G_k^{\mathrm{W}}(t_n - t_i) f_k(t_{i-1})}{2} + \frac{\left[G_k^{\mathrm{W}}(t_n - t_i) - G_k^{\mathrm{W}}(t_n - t_{i-1}) \right] \left[f_k(t_i) - f_k(t_{i-1}) \right]}{3} \right\} \cdot \\ &= w_{k0}^{\mathrm{W}}(t_n) - \Delta t \sum_{i=1}^{n} \left\{ \left[\frac{G_k^{\mathrm{W}}(t_n - t_{i-1}) + 2G_k^{\mathrm{W}}(t_n - t_i)}{6} \right] f_k(t_i) + \left[\frac{2G_k^{\mathrm{W}}(t_n - t_{i-1}) + G_k^{\mathrm{W}}(t_n - t_i)}{6} \right] f_k(t_{i-1}) \right\} \end{aligned} \tag{A.3}$$

By letting

$$\begin{aligned} \gamma_k^{\mathrm{W}}(t_n) = {} & \Delta t \sum_{i=1}^{n-1} \left[\frac{G_k^{\mathrm{W}}(t_n - t_{i-1}) + 2G_k^{\mathrm{W}}(t_n - t_i)}{6} \right] f_k(t_i) \\ & + \Delta t \sum_{i=1}^{n} \left[\frac{2G_k^{\mathrm{W}}(t_n - t_{i-1}) + G_k^{\mathrm{W}}(t_n - t_i)}{6} \right] f_k(t_{i-1}) \end{aligned}, \tag{A.4}$$

$$v_k^{\mathrm{W}}(t_n) = \frac{\Delta t}{6} \left[2G_k^{\mathrm{W}}(t_n - t_n) + G_k^{\mathrm{W}}(t_n - t_{n-1}) \right] = \frac{\Delta t}{6} G_k^{\mathrm{W}}(\Delta t), \tag{A.5}$$

then the wheel displacement can be written as

$$w_k^{\mathrm{W}}(t_n) = w_{k0}^{\mathrm{W}}(t_n) - \gamma_k^{\mathrm{W}}(t_n) - v_k^{\mathrm{W}}(t_n) f_k(t_n). \tag{A.6}$$

Similarly, the rail displacement at the kth wheel-rail contact point can be calculated as

$$w_k^{\mathrm{R}}(t_n) = \sum_{j=1}^{M} \int_{-\infty}^{0} G^{\mathrm{R}}(a_k - a_j, a_j + ct_n, t_n - \tau) P_{j0} \mathrm{d}\tau + \sum_{j=1}^{M} \int_{0}^{t_n} G^{\mathrm{R}}(a_k - a_j, a_j + ct_n, t_n - \tau) f_j(\tau) \mathrm{d}\tau, \tag{A.7}$$

which, as in Ref. [16], can be simplified to be

$$w_k^{\mathrm{R}}(t_n) = w_{k0}^{\mathrm{R}}(t_n) + \gamma_k^{\mathrm{R}}(t_n) + \sum_{j=1}^{M} v_{kj}^{\mathrm{R}}(t_n) f_j(t_n), \tag{A.8}$$

where

$$w_{k0}^{\mathrm{R}}(t_n) = u_k^{\mathrm{R}}(t_n) + \frac{\Delta t}{2} \sum_{j=1}^{M} \left\{ \sum_{i=1}^{n} \left[G_{kj}^{\mathrm{R}-}(t_n, t_i) + G_{kj}^{\mathrm{R}-}(t_n, t_{i-1}) \right] \right\} P_{j0}, \tag{A.9}$$

$$u_k^{\mathrm{R}}(t_n) = \Delta t \sum_{j=1}^{M} \left(\sum_{i=1}^{I} \frac{G_{kj}^{\mathrm{R}+}(t_n, t_i) + G_{kj}^{\mathrm{R}+}(t_n, t_{i-1})}{2} \right) P_{j0}, \tag{A.10}$$

$$\begin{aligned} \gamma_k(t_n) = & \frac{\Delta t}{6} \sum_{j=1}^{M} \sum_{i=1}^{n} \left(G_{kj}^{\mathrm{R}-}(t_n, t_i) + 2G_{kj}^{\mathrm{R}-}(t_n, t_{i-1}) \right) f_j(t_{i-1}) \\ & + \frac{\Delta t}{6} \sum_{j=1}^{M} \sum_{i=1}^{n-1} \left(G_{kj}^{\mathrm{R}-}(t_n, t_{i-1}) + 2G_{kj}^{\mathrm{R}-}(t_n, t_i) \right) f_j(t_i) \end{aligned}, \tag{A.11}$$

$$v_{kj}^{\mathrm{R}}(t_n) = \frac{\Delta t}{6} G^{\mathrm{R}}(a_k - a_j, a_j + ct_n, \Delta t), \tag{A.12}$$

$$G_{kj}^{\mathrm{R}+}(t_n, t_i) = G^{\mathrm{R}}(a_k - a_j, a_j + ct_n, t_n + t_i), \tag{A.13}$$

$$G_{kj}^{\mathrm{R}-}(t_n, t_i) = G^{\mathrm{R}}(a_k - a_j, a_j + ct_n, t_n - t_i). \tag{A.14}$$

According Eq. (A.12), $v_{kj}^{\mathrm{R}}(t_n) = 0$ if $k \neq j$. This is because Δt is so small that the disturbance at a wheel-rail contact point has no time to arrive at another wheel-rail contact point. Thus, Eq. (11) becomes

$$\begin{aligned} & w_{k0}^{\mathrm{W}}(t_n) - \gamma_k^{\mathrm{W}}(t_n) - v_k^{\mathrm{W}}(t_n) f_k(t_n) - w_{k0}^{\mathrm{R}}(t_n) - \gamma_k^{\mathrm{R}}(t_n) - v_{kk}^{\mathrm{R}}(t_n) f_k(t_n) + z_k(a_k + ct_n) \\ & = C_k (P_{k0} + f_k(t_n))^{2/3} \end{aligned}, \tag{A.15}$$

where $k = 1, 2, \ldots M$. By letting,

$$b_k(t_n) = w_{k0}^{\mathrm{W}}(t_n) - \gamma_k^{\mathrm{W}}(t_n) - w_{k0}^{\mathrm{R}}(t_n) - \gamma_k^{\mathrm{R}}(t_n) + z_k(a_k + ct_n), \tag{A.16}$$

$$d_k(t_n) = -v_k^{\mathrm{W}}(t_n) - v_{kk}^{\mathrm{R}}(t_n), \tag{A.17}$$

Eq. (A.15) becomes

$$b_k(t_n) + d_k(t_n) f_k(t_n) = C_k (P_{k0} + f_k(t_n))^{2/3}, \; k = 1, 2, ..., M \tag{A.18}$$

According to the equations established above, an iteration process can be set up to determine the wheel-rail forces and displacements at each time step. In order to start the iteration process, initial values should be given. It is assumed that all the velocities and dynamic wheel-rail forces are vanishing at the moment $t_0 = 0$, but the rail displacement is set to be (see Eq. (A.10))

$$w_k^{\mathrm{R}}(t_0) = w_{k0}^{\mathrm{R}}(t_0) = \Delta t \sum_{j=1}^{M} \left(\sum_{i=1}^{I} \frac{G_{kj}^{\mathrm{R}+}(t_n, t_i) + G_{kj}^{\mathrm{R}+}(t_n, t_{i-1})}{2} \right) P_{j0} \ . \tag{A.19}$$

The initial value of the wheel displacement can be obtained from the following equation,

$$w_k^{\mathrm{W}}(t_0) = w_{k0}^{\mathrm{R}}(t_0) + C_k (P_{k0})^{2/3} . \tag{A.20}$$

With these initial values, the steady-state wheel-rail forces can be obtained by solving the non-linear equations (A.18) for a sufficiently large number of iterations.